

Controlled polymorphic competition – a path to tough and hard ceramics

D.G. Sangiovanni,^{1*} A. Kjellén,¹ F. Trybel,¹ L.J.S. Johnson,² M. Odén,¹
F. Tasnádi,¹ I.A. Abrikosov¹

¹ Department of Physics, Chemistry, and Biology (IFM), Linköping University, SE 58183 Linköping, Sweden

² Sandvik Coromant, 126 80 Stockholm, Sweden

From nanoscale devices including sensors, electronics, or biocompatible coatings to macroscale structural, automotive or aerospace components, fundamental understanding of plasticity and fracture can guide the realization of materials that ensure safe and durable performance. Identifying the role of atomic-scale plasticity is crucial, especially for applications relying on brittle ceramics. Here, stress-intensity-controlled atomistic simulations of fracture in cubic $\text{Ti}_{1-x}\text{Al}_x\text{N}$ model systems demonstrate how \AA -scale plasticity — manifested as lattice distortions, phase transformation, nucleation and emission of dislocations — substantially affects the *macroscale* fracture toughness (K_{Ic}) and fracture strength (σ_f) of brittle ceramics. The extent of plastic deformation in $\text{Ti}_{1-x}\text{Al}_x\text{N}$ increases monotonically with the Al content (x), due to a corresponding decrease in cubic \rightarrow hexagonal polymorph transition energy. Overall, plasticity positively affects the mechanical properties, resulting in optimal combinations of strength and toughness for $x \approx 0.6$. However, for x exceeding ~ 0.7 , the benefits of plasticity diminish. The initial rise followed by a decline in $K_{\text{Ic}}(x)$ and $\sigma_f(x)$ is explained based on the interplay between phase transformation and tensile cleavage on the easiest fracture plane. The results highlight the impact of atomic-scale plasticity on observable properties and point to strategies for toughening ceramics through control of polymorph competition.

*davide.sangiovanni@liu.se

1. Introduction

Ceramics are indispensable for technologies that demand a combination of high hardness, heat tolerance, and good chemical inertness. Unfortunately, they are often characterized by a tendency to fracture before yielding. Brittleness is a problem of major concern, especially in safety-critical applications. In contrast to most ceramics, zirconia (ZrO_2) and ZrO_2 -based alloys [1] display exceptional resistance to fracture, with measured fracture toughness values (K_{Ic}) up to $20 \text{ MPa} \sqrt{\text{m}}$ [2-4]. Such unusual mechanical behavior stems from stress-activated phase transformation ahead of growing cracks, which effectively prevents crack propagation [5-7]. However, the relatively low hardness ($H \approx 10 \text{ GPa}$ [3, 8, 9]) and rapid softening with temperature [8-10] makes ZrO_2 -based alloys unsuited for many ceramics or refractory applications.

The tetragonal-to-monoclinic transition responsible for transformation-toughening in ZrO_2 -based ceramics is accompanied by an anisotropic volumetric strain and shear deformation [11]. At room temperature, the transformation is driven by stress, with transition enthalpies of the order of few tens of meV/atom [12, 13]. These characteristics suggest that control of the thermodynamic competition between polymorph phases can allow designing refractory ceramics with high hardness combined to improved toughness. The design concept is verified here for transition-metal nitride (TMN) alloys.

TMN ceramics are widely applied as protective thin-film coatings on, e.g., cutting tools, engine components, and medical instruments due their high hardness ($H \approx 20 - 45 \text{ GPa}$ [14-16]), fracture strength ($\sigma_f \approx 2 - 6 \text{ GPa}$ [17-20]), and good chemical stability. Similar to other refractory materials, they are characterized by brittleness and low toughness ($K_{Ic} \approx 1 - 5 \text{ MPa} \sqrt{\text{m}}$ [16]). For our analysis, we consider rocksalt-structured (B1) pseudobinary $\text{Ti}_{1-x}\text{Al}_x\text{N}$ solid solutions as representative model systems because Al substitutions enable tuning of the

competition between different polymorphs within a relatively narrow energy range [21, 22].^[f1] Furthermore, experiments have shown that AlN-containing alloys and superlattices exhibit improved fracture resistance [28-30], phenomenologically attributed to stress-activated transformation plasticity in AlN-rich domains [28-30].

Processes that govern plasticity and fracture are often beyond the spatial and/or time resolution of electron microscopy. Experimental identification of nanoscale plasticity becomes even more complex for thin-film coatings, such as $Ti_{1-x}Al_xN$ [31, 32], due to small sample sizes and substrate effects. We employ atomistic simulations implemented with stress-intensity-controlled deformation of defective crystal models to characterize the fracture strength and fracture toughness of $Ti_{1-x}Al_xN$ ceramics. The availability of experimental fracture properties – measured by $Ti_{1-x}Al_xN$ microcantilever bending and micropillar splitting over a wide compositional range – allows supporting theoretically-determined trends and hence ascribing the observed toughening and strengthening effects to plasticity at the atomic scale.

2. Results and discussion

Atomistic simulations of fracture are performed using molecular statics (MS) based on the modified embedded-atom method (MEAM) parameterized for Ti-Al-N systems [33]. Predictive accuracy in calculated fracture properties can be assured by controlling the stress intensity factor (K_I) at the crack tip of a defective lattice while also verifying that inelastic processes are confined to a relatively small region centered at the tip [34]. Mode-I (crack-opening) and mode-II (shearing) loading based on anisotropic elasticity has been implemented in our previous study on the competition between dislocation emission and crack propagation in TiN_x [35]. Here, we investigate B1 $Ti_{1-x}Al_xN$ ($0 \leq x \leq 0.95$) crystal models that contain an

^[f1] Note that B1 (Ti,Al)N solid solutions are thermodynamically inclined to decompose spinodally into cubic AlN-rich/TiN-rich coherent domains [23]. However, spinodal decomposition is kinetically-prevented by very low atomic diffusivities in nitrides [24–27].

atomically sharp crack on the (001) or on the (111) plane. Below, the defective lattices with different crack geometry are indicated as $\text{Ti}_{1-x}\text{Al}_x\text{N}(001)$ or $\text{Ti}_{1-x}\text{Al}_x\text{N}(111)$. We note that atomically-sharp cracks have been experimentally observed in diverse material systems [36-39]. **Section S1** of the **Supporting Information (SI)** details supercell models and methods used in atomistic simulations of fracture.

2.1. Potential validation against *ab initio* results for notched lattice models

The classical MEAM potential – as parameterized in Ref. [33] – has been proven to reproduce experimental and *ab initio* properties of defect-free and defective TiN and Ti-Al-N alloys, including their different polymorph structures [35, 40-42]. The interested reader may consult **Section S2 of the SI** for detailed information on properties and phenomena that have been tested and validated. To verify that the MEAM classical potential can realistically describe plastic deformation and fracture in $\text{Ti}_{1-x}\text{Al}_x\text{N}$ alloys (prior to carrying out computationally-intensive K_I -controlled simulations), we compare the results of classical (CMD) and *ab initio* molecular dynamics (AIMD) obtained for small, notched supercell models subjected to $\langle 001 \rangle$ tensile elongation. Besides serving for validation of the MEAM model, the simulations allow us to rapidly probe the tendency of B1 $\text{Ti}_{1-x}\text{Al}_x\text{N}$ alloys to deform plastically.

CMD and AIMD results of deformed notched $\text{Ti}_{0.5}\text{Al}_{0.5}\text{N}$ and $\text{Ti}_{0.25}\text{Al}_{0.75}\text{N}$ models are presented in **Figure 1**. Our previous simulations showed that notched TiN fractures in a brittle manner at $\sim 30\%$ tensile strain of the simulation box (figure 5 in [35]). At the same elongation, B1 $\text{Ti}_{0.5}\text{Al}_{0.5}\text{N}$ and $\text{Ti}_{0.25}\text{Al}_{0.75}\text{N}$ undergo lattice transformation around the notches (**Figure 1**). The observed structural changes preserve the integrity of the bonding network, thus indicating that $\text{Ti}_{0.5}\text{Al}_{0.5}\text{N}$ and $\text{Ti}_{0.25}\text{Al}_{0.75}\text{N}$ are qualitatively more plastic and resistant to fracture than TiN. The lattice distortions seen in $\text{Ti}_{0.5}\text{Al}_{0.5}\text{N}$, resemble the initial stage of cubic B1 \rightarrow hexagonal B_k transformation (see orange circles and dotted lines in **Figure 1a,c**). For the case of notched $\text{Ti}_{0.25}\text{Al}_{0.75}\text{N}$, a strain of 50% leads to the formation of B_k-structured domains

(**Figure 1b,c**). The B_k phase (hexagonal BN prototype) is a honeycomb-patterned variant of the hexagonal wurtzite (B_4) structure in which metal and N atoms of adjacent (0001) layers shift onto the same lattice plane (**Figure S8**). Accordingly, during $B_1 \rightarrow B_k$ phase transformation, the atomic coordination decreases from six- to five-fold.

The formation of B_k -structured domains in strained notched $Ti_{1-x}Al_xN$ models is surprising, as the B_k phase has (to the best of our knowledge) not been previously detected in $Ti_{1-x}Al_xN$ samples. Reports in the literature show that $Ti_{1-x}Al_xN$ films with compositions $x \gtrsim 0.7$ often exhibit a dual phase ($B_1 + B_4$) or single phase (B_4) structure [43].^[f2] Oppositely, $Ti_{1-x}Al_xN$ films with Al contents $x < 0.7$ are typically single-phase B_1 [31]. The experimental findings are consistent with the results of density-functional theory (DFT) calculations indicating that $Ti_{1-x}Al_xN$ solid solutions energetically favor the B_4 (or B_1) structure for Al contents greater (or lower) than ~ 0.7 [21]. DFT investigations also demonstrated that the B_4 phase is mechanically unstable for alloys with $x \lesssim 0.6$ [43], and relax into the B_k during structural optimization [45]. Thus, previous DFT results [21, 43, 45] clarify why B_k domains can form in B_1 $Ti_{0.5}Al_{0.5}N$ under loading (**Figure 1a**). The appearance of B_k (instead of B_4) environments in strained $Ti_{0.25}Al_{0.75}N$ (**Figure 1b**) is even less expected than in $Ti_{0.5}Al_{0.5}N$. Our simulations suggest that the B_k phase is stabilized through tensile elongation. The hypothesis is confirmed by complementary DFT and MS calculations showing that [1120]-elongated B_4 $Ti_{0.25}Al_{0.75}N$ transforms into B_k -structured $Ti_{0.25}Al_{0.75}N$ (**Figure S9**). The results emphasize the relevance of B_k domains in plastically deformed regions of Al-rich $Ti_{1-x}Al_xN$ ceramics.

The agreement between AIMD and CMD results of stress-activated transformation in notched lattices, together with the extensive validation presented in **Section S1 of the SI**, lends

^[f2] $Ti_{1-x}Al_xN$ films synthesized by physical vapor deposition exhibit single-phase B_1 structure for x up to ~ 0.7 [31]. However, results of experiments based on chemical vapor deposition indicated that single-phase B_1 $Ti_{1-x}Al_xN$ solid solutions can be realized with Al contents as high as ~ 0.9 [32], [44].

confidence that the MEAM force field can realistically describe plasticity and fracture processes in $\text{Ti}_{1-x}\text{Al}_x\text{N}$.

2.2. Influence of polymorphic transformation on properties of B1 $\text{Ti}_{1-x}\text{Al}_x\text{N}(001)$

K_I -controlled simulations of fracture are carried out for cracked-plate supercell models containing up to 1.3 million atoms; a size deemed sufficient to reliably extrapolate macroscale properties (details in **Section S1 of the SI**). Simulations performed for $\text{Ti}_{1-x}\text{Al}_x\text{N}$ are repeated with different stochastic cation arrangements to gain reasonable statistical confidence on $K_{Ic}(A)$ and $\sigma_f(A)$ values for each plate area (A) considered here. The constitutive scaling laws identified in this work reproduce $K_{Ic}(A)$ and $\sigma_f(A)$ vs. A asymptotic trends, and allow us to extrapolate the material fracture toughness K_{Ic}^∞ and fracture strength σ_f^∞ (intended as crack-initiation toughness and strength) at the macroscale limit. Such *macroscale* properties unambiguously characterize the mechanical behavior of B1 $\text{Ti}_{1-x}\text{Al}_x\text{N}$ with well-defined crack geometries. The properties measured for actual $\text{Ti}_{1-x}\text{Al}_x\text{N}$ samples are, instead, affected by mechanical-testing parameters and the structure, properties, and density of extended crystallographic defects.

The results of K_I -controlled deformation show that the mechanical properties of B1 $\text{Ti}_{1-x}\text{Al}_x\text{N}(001)$ and $\text{Ti}_{1-x}\text{Al}_x\text{N}(111)$ cracked plates vary with x in a qualitatively similar manner. We choose to focus on description of the properties of $\text{Ti}_{1-x}\text{Al}_x\text{N}(001)$ systems, as the $\{001\}$ surfaces are often the most stable in B1 structured ceramics [46-48] and thus expected to be the easiest fracture planes. Noteworthy differences between the behaviors of cracks on (001) and (111) planes, and associated plastic deformation mechanisms, are described in **Section 2.3**.

Figure 2a and 2c report the values of K_{Ic}^∞ and σ_f^∞ obtained for B1 $\text{Ti}_{1-x}\text{Al}_x\text{N}(001)$ alloys. All simulations carried out for B1 $\text{TiN}(001)$ evidence crack extension along the (001) plane (**Video #1**). The mechanical properties of $\text{TiN}(001)$ extrapolated to the macroscale limit are $K_{Ic}^\infty \approx 1.8 \text{ MPa } \sqrt{\text{m}}$ and $\sigma_f^\infty \approx 2.4 \text{ GPa}$. As anticipated by results obtained for the small, notched lattice models in **Figure 1**, Al substitutions improve the resistance to fracture of Ti_{1-}

$x\text{Al}_x\text{N}$ alloys. **Figure 2a,c** show a monotonic rise in the K_{Ic}^∞ and σ_f^∞ values for an aluminum content x increasing from 0 to 0.6. Accordingly, B1 $\text{Ti}_{0.4}\text{Al}_{0.6}\text{N}(001)$ shows the best combination of toughness ($3.2 \text{ MPa } \sqrt{\text{m}}$) and strength (4.3 GPa). As clarified below, the enhancement in fracture resistance is due to lattice distortions localized around the crack tip and extrinsic toughening mechanisms. A further increase in aluminum concentration becomes less advantageous for the mechanical properties of $\text{Ti}_{1-x}\text{Al}_x\text{N}$ alloys. The effect is indicated by reductions in K_{Ic}^∞ and σ_f^∞ for x greater than 0.7 (**Figure 2a,c**). The deterioration in mechanical properties in Al-rich B1 $\text{Ti}_{1-x}\text{Al}_x\text{N}$ is caused by premature $\text{B1} \rightarrow \text{B}_k$ phase transformation, activated under loading.

We should note that the formation of a secondary phase in the cubic host lattice introduces an uncertainty on K_{Ic} and σ_f values predicted for B1-structured $\text{Ti}_{1-x}\text{Al}_x\text{N}$ alloys with $x > 0.7$. The definition of K_I becomes progressively less accurate as the hexagonal phase grows within the B1 lattice.^[f3] Nevertheless, the *true* fracture toughness and strength of B1 $\text{Ti}_{1-x}\text{Al}_x\text{N}$ with $x > 0.7$ are expected to be close to the values of **Figure 2a,c**. Our claim is motivated by the fact that the K_I -controlled simulations are terminated when the fractional advancement of the crack front (Δ_{tip}), or extension of the secondary phase, has reached 5% of the plate model size (details in **Section 5.3**). Through separate analyses (not shown), we verify that setting a Δ_{tip} parameter below 5% does not alter the trends in mechanical properties as a function of the Al content. Additionally, the K_{Ic}^∞ and σ_f^∞ values of B1-structured alloys calculated for $0 < \Delta_{\text{tip}} < 5\%$ remain close to the confidence ranges shown in **Figure 2a,c**. An accurate determination of the properties of dual-phase $\text{Ti}_{1-x}\text{Al}_x\text{N}$ is beyond the scope of this work. However, complementary K -controlled simulations demonstrate that single-phase B_k -structured $\text{Ti}_{0.25}\text{Al}_{0.75}\text{N}$ and $\text{Ti}_{0.15}\text{Al}_{0.85}\text{N}$ are considerably less resistant to fracture than the corresponding

^[f3] The K_I is controlled through atomic displacements that are, in turn, calculated from the elastic response of the original untransformed cubic phase.

cubic crystals (see **Figure 2a,c**, **Figure S11**, and **Videos #2 and #3**). Thus, the relatively high fracture toughness of B1 $\text{Ti}_{0.25}\text{Al}_{0.75}\text{N}(001)$ and $\text{Ti}_{0.15}\text{Al}_{0.85}\text{N}(001)$ are partially compromised by local transformations into the weaker B_k phase.

The impact of atomic-scale transformation on the material's resistance to fracture can be assessed by comparing K_{Ic}^{∞} results of atomistic simulations (**Figure 2a**) with Griffith's K_{Ic}^{G} values (**Figure 2b**). The latter are predicted from linear elastic fracture mechanics (LEFM). In LEFM, a solid is assumed to maintain a linear elastic response up to fracture (see **Section S2 in the SI**). Therefore, while a ratio $K_{\text{Ic}}^{\infty}/K_{\text{Ic}}^{\text{G}} \approx 1$ would correspond to perfectly brittle fracture, a $K_{\text{Ic}}^{\infty}/K_{\text{Ic}}^{\text{G}} \gg 1$ indicates that inelastic effects greatly contribute to the toughness. According to LEFM, the fracture toughness of B1 $\text{Ti}_{1-x}\text{Al}_x\text{N}(001)$ would (misleadingly) decrease with increasing x (**Figure 2b**). The trends in K_{Ic}^{G} vs. x obtained by MEAM are confirmed by DFT calculations (**Figure 2b**). On the contrary, K_{Ic}^{∞} results in **Figure 2a** demonstrate that Al substitutions have positive effects on the alloys' resistance to fracture, at least for x up to ≈ 0.6 . The ratio $K_{\text{Ic}}^{\infty}/K_{\text{Ic}}^{\text{G}}$ (not plotted) increases monotonically from 1.2 ± 0.1 (in brittle B1 $\text{TiN}(001)$) to 2.5 ± 0.2 for B1 $\text{Ti}_{0.4}\text{Al}_{0.6}\text{N}(001)$, which is the toughest and strongest of the alloys tested in this work. The deviations between K_{Ic}^{∞} and K_{Ic}^{G} trends qualitatively demonstrate the significant contribution of atomic-scale plasticity on the fracture toughness of the alloy.

Our simulations show that the extent of plastic deformation in B1 $\text{Ti}_{1-x}\text{Al}_x\text{N}(001)$ subjected to mode-I loading increases monotonically with the Al concentration. The effect is evidenced by structural analyses of $\text{Ti}_{1-x}\text{Al}_x\text{N}(001)$ cracked-plate models at a stress intensity factor $K_{\text{I}} = 2 \text{ MPa } \sqrt{\text{m}}$ (**Figure 3b-g**). The results obtained for notched models in **Figure 1** suggest that plasticity in mode-I loaded B1 $\text{Ti}_{1-x}\text{Al}_x\text{N}(001)$ lattices is dominated by the formation of B_k -like domains. The tension-driven $\text{B1} \rightarrow \text{B}_k$ transformation path is represented in **Figure 1c**. Accordingly, the degree of plasticity should be inversely related to the polymorphic transition energy ($\Delta E_{\text{B1} \rightarrow \text{B}_k}$). The correlation between the degree of plasticity and

$\Delta E_{B1 \rightarrow B_k}^{-1}$ is shown in **Figure 3a**, where both quantities increase monotonically with the Al concentration x .

Irrespective of their size, TiN crystal models containing an atomically-sharp (001) crack undergo cleavage fracture when subjected to mode-I loading (**Figure 3b,b'**). However, as shown by results in **Figure 2a,c**, both strength and toughness can be enhanced by wisely tuning the metal composition. While a small addition of Al ($x \lesssim 0.25$) in $\text{Ti}_{1-x}\text{Al}_x\text{N}(001)$ leads to relatively small improvements in fracture resistance (**Figure 3c,c'**), an Al content up to 0.6 induces progressively more pronounced structural distortions at the crack tip (**Figure 3d,d'**), which retards fracture by locally redistributing and/or dissipating stress. The enhanced resistance to crack propagation for x increasing from 0 to 0.6 is demonstrated by a slower crack-tip advancement Δ_{tip} as a function of K_I (**Figure S10b**).

The mechanism for Al-mediated toughening and strengthening is detailed in **Figure 4**, where B1 $\text{Ti}_{0.4}\text{Al}_{0.6}\text{N}(001)$ is taken as representative case. **Figure 4a** and its magnification shows puckering of atomic layers around the crack tip. The corrugated portion of the $\text{Ti}_{0.4}\text{Al}_{0.6}\text{N}(001)$ lattice resembles B_k -like environments encountered along the $B1 \rightarrow B_k$ transformation path. At the same time, the alloy undergoes amorphization at the crack tip (**Figure 4a**). A further increase in load does not lead to a complete transformation, but rather initiates fracture. Nevertheless, the crack propagates relatively slowly in $\text{Ti}_{0.4}\text{Al}_{0.6}\text{N}(001)$ thanks to the formation of ligaments connecting opposite surfaces behind the crack tip (**Figure 4b and 4c**). The dark blue color indicate that these “atomic bridges” carry substantial tensile load (**Figure 4b and 4c**) and are therefore responsible for extrinsic toughening (crack-growth toughness [49]) of $\text{Ti}_{0.4}\text{Al}_{0.6}\text{N}(001)$. A similar phenomenon has been observed experimentally and proposed as toughening effect in other nitride ceramics [50].

Although the calculated toughness and strength of $\text{Ti}_{1-x}\text{Al}_x\text{N}(001)$ initially rise with x (**Figure 2a,c**), the white-gray color gradient in **Figure 3a** marks the compositional limit where

the effects of plasticity on mechanical properties start becoming less beneficial. Indeed, **Figure 2a,c** evidences a decline in K_{Ic}^{∞} and σ_f^{∞} for $x \gtrsim 0.7$. The reduction in strength and toughness originates from early mechanical yielding caused, in turn, by premature nucleation and growth of the weaker hexagonal B_k polymorph. The phenomenon is exemplified for the case of $Ti_{0.15}Al_{0.85}N(001)$ in **Figure 5**. When subjected to mode-I loading, the B1 structure starts transforming into B_k at a relatively low stress intensity factor ($K_I \approx 1.3 \text{ MPa} \sqrt{\text{m}}$). We thus infer that an early onset of phase transformation (especially if extended) is detrimental for the alloy's strength and toughness. The scenario would qualitatively change if the newly formed phase were inherently stronger and tougher than the parent phase. This is the case for $Ti_{0.05}Al_{0.95}N(001)$, where the hexagonal structure exhibits better properties than the cubic one (**Figure 2a,c**). In absolute terms, however, $Ti_{0.05}Al_{0.95}N(001)$ alloys are predicted to possess relatively low toughness and strength (**Figure 2a,c**).

The trends in mechanical properties shown in **Figure 2a,c** can be rationalized from the competition between the polymorphic transition energy $\Delta E_{B1 \rightarrow Bk}$ and the energy (γ_f) required to cleave defect-free B1 $Ti_{1-x}Al_xN(001)$ crystals during [001] uniaxial elongation. The quantities $\Delta E_{B1 \rightarrow Bk}$ and γ_f – readily obtained by static calculations of 3D periodic $Ti_{1-x}Al_xN$ supercells – are here identified as useful descriptors for the complex mechanical behavior of the alloy during mode-I loading. Hence, $Ti_{1-x}Al_xN$ lattice models with low, intermediate, and high Al contents are considered as representative cases to probe the effect of composition on the energetic tendency for brittle fracture or phase transformation. We compare energy trends computed during sequential [001]-elongation and stepwise deformation along the $B1 \rightarrow B_k$ transformation path of **Figure 1c**. Details on the approach are given in **Section S3 of the SI**.

Considering the case of TiN – the most brittle among all systems studied here – **Figure 6a** shows that uniform uniaxial strain up to (001) cleavage is energetically favored over lattice transformation throughout the deformation process. The result is consistent with the

observation that TiN(001) preserves octahedral B1-like coordination up to fracture during mode-I loading simulations (**Figure 3b,b' and Video #1**). Expressed in more general terms, for TiN(001) or $\text{Ti}_{1-x}\text{Al}_x\text{N}(001)$ with relatively low ($x \lesssim 0.3$) Al content, the energy required to activate transformation considerably exceeds the (001) cleavage energy γ_f (**Figure 6d**). The large gap between γ_f and $\Delta E_{\text{B1} \rightarrow \text{Bk}}$ aids our understanding for why these alloys exhibit rapid crack propagation during K_I -controlled simulations. Aluminum-rich ($x \gtrsim 0.7$) $\text{Ti}_{1-x}\text{Al}_x\text{N}$ solid solutions display a diametrically opposite behavior. The energy accumulated by straining along the $\text{B1} \rightarrow \text{Bk}$ transformation path is constantly below the uniaxial elongation energy, as exemplified by results of $\text{Ti}_{0.15}\text{Al}_{0.85}\text{N}$ in **Figure 6c**. The fact that $\Delta E_{\text{B1} \rightarrow \text{Bk}} < \gamma_f$ for $x \gtrsim 0.7$ (**Figure 6d**) may explain the tendency of $\text{Ti}_{1-x}\text{Al}_x\text{N}(001)$ alloys with high Al content to phase-transform before fracturing (see, e.g., **Figure 5**). Transformation plasticity would be obviously desirable if the newly formed phase were stronger than the original crystal structure. This is however not the case for $\text{Ti}_{0.25}\text{Al}_{0.75}\text{N}(001)$ and $\text{Ti}_{0.15}\text{Al}_{0.85}\text{N}(001)$, as the hexagonal lattice is weaker than the cubic one (**Figure 2a,c**). The crack front of alloys with intermediate Al concentrations undergoes a relatively slow and localized modification of the bonding network during K_I -controlled loading (see results of $\text{Ti}_{0.4}\text{Al}_{0.6}\text{N}(001)$ in **Figure 4a**). For Al concentrations $x \approx 0.6$, the values of tensile cleavage fracture γ_f are slightly lower than $\Delta E_{\text{B1} \rightarrow \text{Bk}}$ (**Figure 6b,d**). This suggests that alloys with intermediate Al contents can accommodate higher amounts of mechanical energy by lattice distortions before fracturing, which has an optimal effect on strength and toughness (**Figure 2a,c**).

2.3. Effects of stacking-fault formation on fracture resistance of B1 $\text{Ti}_{1-x}\text{Al}_x\text{N}(111)$

The effect of polymorphic competition on the mechanical properties of $\text{Ti}_{1-x}\text{Al}_x\text{N}$ ceramics is analyzed further by investigating fracture mechanisms in alloy models containing (111) cracks. MS simulations reveal that the mechanical response of $\text{Ti}_{1-x}\text{Al}_x\text{N}(111)$ alloys changes – from brittle to progressively more plastic – with increasing Al concentration,

consistent with observations made for $\text{Ti}_{1-x}\text{Al}_x\text{N}(001)$. The trends in K_{Ic}^∞ and σ_f^∞ calculated for $\text{Ti}_{1-x}\text{Al}_x\text{N}(111)$ as a function of x are alike those of $\text{Ti}_{1-x}\text{Al}_x\text{N}(001)$, as indicated by black squares and purple triangles in **Figure 7**. Maximum toughness and strength of $\text{Ti}_{1-x}\text{Al}_x\text{N}(111)$ are recorded for Al concentrations around 0.6. It is, however, worth noting that the fracture toughness values calculated for $\text{Ti}_{1-x}\text{Al}_x\text{N}(001)$ are systematically lower (between ~10 and 30%) than those obtained for $\text{Ti}_{1-x}\text{Al}_x\text{N}(111)$ (**Figure 7a**). In contrast, the theoretical fracture strength of B1 $\text{Ti}_{1-x}\text{Al}_x\text{N}$ appears relatively unaffected by the orientation of the crack plane, as indicated by the overlapping error bars of square and triangular symbols in **Figure 7b**.

Although $\text{Ti}_{1-x}\text{Al}_x\text{N}(001)$ and $\text{Ti}_{1-x}\text{Al}_x\text{N}(111)$ cracked-plate models return similar trends in mechanical properties, they also exhibit some remarkable differences in fracture mechanisms. Mode-I loading of $\text{TiN}(111)$ reveals that (111) cracks are readily deflected along (001) planes (**Figure 8a**). The phenomenon is observed for all $\text{TiN}(111)$ plate areas tested here. This suggests that the crack paths in TiN constantly follow the lowest-energy surface. In $\text{Ti}_{0.75}\text{Al}_{0.25}\text{N}(111)$ models, the crack wake exhibits a zig-zag pattern formed of (111) and (001) nanofacets (**Video #4**). The toughness and strength of $\text{Ti}_{0.75}\text{Al}_{0.25}\text{N}(111)$ are slightly improved compared to $\text{TiN}(111)$, presumably due to formation of ligaments that slow down crack extension. A further increase in Al concentration progressively promotes nucleation and emission of dislocations from the crack tip of $\text{Ti}_{1-x}\text{Al}_x\text{N}(111)$. In $\text{Ti}_{0.4}\text{Al}_{0.6}\text{N}(111)$, the mechanism leads to formation of a stacking fault on the $(1\bar{1}1)$ plane, inclined 70.5° to the (111) crack surface, as indicated by the orange circle in **Figure 8b**. Slip-induced plastic deformation blunts the crack, thus relieving the high tip stress and enhancing the material resistance to fracture. However, an Al content greater than ~0.7 onsets plastic deformation at a “too” early stage of loading, which has a less positive effect on the mechanical properties of B1 $\text{Ti}_{1-x}\text{Al}_x\text{N}(111)$. This is reflected by a decline in the K_{Ic}^∞ and σ_f^∞ for $x > 0.7$ (**Figure 7a,b**). Specifically, $\text{Ti}_{0.25}\text{Al}_{0.75}\text{N}(111)$ nucleates and emits the first dislocation at $K_I \approx 2.1 \text{ MPa} \sqrt{\text{m}}$.

The event triggers a rapid sequence of dislocation glides (avalanche emission), effectively resulting in the formation of hexagonal (mainly B4-structured) domains (**Figure S12**).

Simulations done for crystal models with (001) and (111) cracks highlight that $\text{Ti}_{1-x}\text{Al}_x\text{N}$ alloys become more plastic with an increasing concentration of aluminum. In $\text{Ti}_{1-x}\text{Al}_x\text{N}(001)$, plastic deformation is primarily manifested through localized lattice distortions, amorphization, and phase transformation. In $\text{Ti}_{1-x}\text{Al}_x\text{N}(111)$, the predominant mechanism for toughening and strengthening are the nucleation and emission of dislocations along $(1\bar{1}1)$ planes, resulting in the formation of stacking faults. We have indeed shown by MS calculations and experiments that the energy of formation of (111) stacking faults in $\text{Ti}_{1-x}\text{Al}_x\text{N}$ decreases with an increasing aluminum content: $1.43 \text{ J}\cdot\text{m}^{-2}$ for TiN, $1.0\pm 0.2 \text{ J}\cdot\text{m}^{-2}$ for $\text{Ti}_{0.4}\text{Al}_{0.6}\text{N}$, and $0.7\pm 0.3 \text{ J}\cdot\text{m}^{-2}$ for $\text{Ti}_{0.25}\text{Al}_{0.75}\text{N}$ [51]. Likewise, the *unstable* stacking fault energy – a critical parameter for predicting Mode-I dislocation emission in Rice model [52] – decreases monotonically with increasing x . The reduction in stacking fault energies, leading to an increased ability of the alloys to slip on (111) planes, is the manifestation of a lower activation energy for cubic-to-hexagonal polymorphic transformation.

2.4. Comparison with experimental fracture properties

Besides showing simulation results, **Figure 7** reports literature values of fracture toughness (K_{Ic}^{exp}) and fracture strength (σ_f^{exp}) measured for TiN and $\text{Ti}_{1-x}\text{Al}_x\text{N}$ coatings by microcantilever bending and micropillar splitting. The experimental values were collected for as-deposited $\text{Ti}_{1-x}\text{Al}_x\text{N}$ coatings with metal/N stoichiometry near unity (K_{Ic}^{exp} : [17-19, 30, 53-60] and σ_f^{exp} : [18, 19, 53-55]). Mechanical properties assessed by nanoindentation are omitted from the figure due to the bias introduced by residual film stresses [61] and mixed type of loading (compressive, tensile, shear) near indented regions [62].

The trends in fracture toughness and fracture strength determined by atomistic simulations are consistent with experiments (**Figure 7**). The properties measured for TiN are

scattered over a relatively wide range: $K_{Ic}^{exp} \sim 1 - 3.5 \text{ MPa } \sqrt{\text{m}}$ and $\sigma_f^{exp} \sim 1.5 - 5 \text{ GPa}$; effect that could be due to samples with different average grain sizes [63] or different microstructural quality. Nevertheless, the results of simulations done on TiN models with (001) and (111) cracks ($K_{Ic}^{\infty} = 1.84 \pm 0.03$ and $2.59 \pm 0.12 \text{ MPa } \sqrt{\text{m}}$; $\sigma_f^{\infty} = 2.37 \pm 0.13$ and $2.54 \pm 0.18 \text{ GPa}$) are within the confidence ranges of the mean experimental values ($K_{Ic}^{exp} = 2.3 \pm 0.7 \text{ MPa } \sqrt{\text{m}}$; $\sigma_f^{exp} = 3.1 \pm 1.0 \text{ GPa}$). Consistent with the theoretical trends, the K_{Ic}^{exp} and σ_f^{exp} determined for $Ti_{1-x}Al_xN$ exhibit maxima for x around 0.6. Similarly, the machining performance and lifetime of $Ti_{1-x}Al_xN$ -coated cutting tools increases monotonically with the concentration of Al up to $x \sim 0.6-0.7$ (see figure 7 in Ref. [64]).

In general, the fracture toughness and strength measured for polycrystalline samples cannot be compared directly to properties calculated for single-crystals. While our models elucidate transgranular fracture mechanisms, ex-situ (post-mortem) microscopy cannot reveal whether failure of $Ti_{1-x}Al_xN$ occurred intergranularly or transgranularly [56, 65]. On the other hand, the calculated K_{Ic} and σ_f trends are consistent with experiments (**Figure 7**). This suggests that atomic-scale plasticity and polymorphic competition largely control the fracture properties of $Ti_{1-x}Al_xN$ ceramics, irrespective of whether fracture is intergranular or transgranular. To support this argument, we present an analysis of the properties of grain boundaries in B1 $Ti_{1-x}Al_xN$ alloys.

The size, relative density, and structure of grain boundaries in B1-structured nitrides, carbides, and oxides vary largely depending on the synthesis parameters [66-73]. However, based on experimental information collected for B1 TMN [74-76], MgO [68, 77], and NiO [67], we can identify three relevant symmetric tilt grain boundaries: $\Sigma 3\{112\}[110]$, $\Sigma 5\{210\}[001]$, and $\Sigma 5\{310\}[001]$ (**Figure S13**). **Table S2 of the SI** shows that the energies (E^{GB}) calculated by MS for the $\Sigma 3$ and $\Sigma 5$ grain boundaries in B1 TiN ($2.70 - 3.29 \text{ J/m}^2$) are in reasonable agreement with previous DFT values ($1.73 - 2.13 \text{ J/m}^2$ [78-82]). Both MS and DFT

results return the relationship: $E_{\Sigma 5\{310\}}^{GB} < E_{\Sigma 5\{210\}}^{GB} < E_{\Sigma 3\{112\}}^{GB}$. K-controlled simulations of grain boundary fracture are beyond the scope of this work. Nevertheless, trends in intergranular fracture toughness assessed using Griffith's criterion indicate that the resistance to fracture of the three boundaries decreases (exception made for $\Sigma 5\{210\}[001]$ in $Ti_{0.25}Al_{0.75}N$) with an increasing concentration of aluminum, as shown in **Table S3**. These results exclude the possibility that the enhancement in toughness and strength observed in experiments for $Ti_{1-x}Al_xN$ with $x \sim 0.6$ arises from a bare improvement of cohesive forces between grains. Irrespective of whether cracks propagate along boundaries or across grains, the agreement between experimental and calculated properties in **Figure 7** indicates that aluminum-induced atomic-scale plasticity can positively affect both the intergranular and transgranular resistance to fracture of actual B1 $Ti_{1-x}Al_xN$ ceramics.

To summarize, this study highlights the positive contribution of atomic-scale plasticity to the fracture resistance of hard ceramics ($H \gtrsim 20$ GPa). The finding challenges the common belief that toughening mechanisms in brittle solids operate primarily at the microscale and that extrinsic toughening is the only route to improve the resistance to fracture of crystalline ceramics [49]. In this regard, recent experimental studies have shown that crystalline ceramics can be intrinsically toughened by artificially increasing the density of native dislocations [83-85]. Our work introduces an alternative strategy that exploits polymorphic competition to regulate phase-transformation toughening at the nano or sub-nano scale.

4. Conclusions

Atomistic simulations of fracture elucidate fundamental mechanisms that control the fracture toughness and fracture strength of $Ti_{1-x}Al_xN$ solid solutions. $Ti_{1-x}Al_xN$ alloys are taken as representative material systems to reveal and understand the effects of atomic-scale plasticity on the fracture properties of hard refractory ceramics. The results evidence that the energetic

competition between polymorphs is a key parameter for controlling the onset and extent of phase transformation plasticity upon loading. Plasticity is shown to generally improve the alloys' resistance to fracture. However, an optimal combination of material strength and toughness is achieved for compositions that lead to moderate plastic deformation, as this allows accommodating a larger amount of mechanical stress prior to fracture.

5. Computational methods

DFT calculations and AIMD simulations are carried out using the VASP code implemented with projector augmented-wave pseudopotentials [86, 87]. In DFT calculations, the energy cutoff of planewaves is set to 400 eV. The thickness of k-point grids used for integration of the reciprocal space varies depending on the property under investigation (details are given in the **SI**). AIMD simulations employ Γ -point sampling of the Brillouin zone and 300 eV cutoff energies. In both DFT and AIMD, the electronic exchange and correlation energies are treated with the approximation of Perdew-Burke-Ernzerhof [88]. For calculations of surface energies at 0 K, we also employ the LDA approximation. Classical molecular dynamics (CMD) and molecular statics (MS) simulations are performed with LAMMPS [89] describing Ti-Al-N interactions based on the second-neighbor modified-embedded atom method (MEAM) [90], as parameterized for Ti-Al-N systems in Ref. [33]. Videos and figures showing atomistic structures are created using VMD [91]. Description of the videos can be found in **Section S4 of the SI**.

5.1. Tensile deformation of notched lattice models. The computational approach used in CMD and AIMD simulations of tensile-testing of small notched lattice models have been detailed in our previous work [35]. The structures contain 1100 atoms with a supercell area of $\approx 13 \text{ nm}^2$ parallel to the [001] strain direction (see **Figure 1**). The simulation box is elongated

up to fracture, incrementing strain by 2% every 1.5 ps. At each strain step, the structures are equilibrated via NVT sampling (300 K) with a timestep of 1 fs.

5.2. K_I-controlled loading of cracked plate models. The method used to carry out K_I controlled simulations of a cracked plate lattice model (schematically illustrated in **Figure S1 of the SI**) has been implemented in our previous study on TiN [35]. The plate models contain an atomically sharp crack on the (001) or on the (111) plane (with crack front along the [010] and [1 $\bar{1}$ 0] crystal axis, respectively) and are periodic along the crack front direction. The (001) surface is the one of lowest formation energy in B1-structured ceramics [46] and is thus expected to be the easiest path for transgranular fracture. Although the (111) surface of B1-structured Ti_{1-x}Al_xN has a much higher formation energy than the (001) [47, 78], the texture of polycrystalline Ti_{1-x}Al_xN PVD coatings is dominated by (001)- and (111)-faceted grains [64, 92-94]. Therefore, fracture during experimental mechanical testing could initiate at nanovoids or flaws with local (111) or (001) surface orientation. In Ti_{1-x}Al_xN(111) plate models, atomically-sharp (111) cracks are created by removing half Ti monolayer, which results in two N-terminated surfaces on opposite sides of the crack plane. The choice is motivated by the fact that N-terminated TiN(111) surfaces are energetically more stable than Ti-terminated (111) surfaces [95]. The stress-intensity factor is incremented stepwise ($\Delta K_I = 0.02 \text{ MPa}\sqrt{\text{m}}$) by controlling the displacement of atoms within the frame region of the plate model [34, 35] (see also **Figure S1**). Crack-healing is prevented by screening the interactions of atoms on opposite sides of the crack plane.

K_I-controlled simulations reveal that B1 Ti_{1-x}Al_xN alloys with Al concentrations $x > 0.7$ undergo phase transformation by nucleation and growth of the B_k hexagonal structure around the crack front. The stress-intensity required to activate such transformation decreases rapidly for Al metal percentage increasing above 70%. This observation requires separate characterization of the mechanical properties of the hexagonal phase. Thus, we compute the

equilibrium structure and elastic tensor of configurationally-disordered B_k $Ti_{0.25}Al_{0.75}N$, $Ti_{0.15}Al_{0.85}N$, and $Ti_{0.05}Al_{0.95}N$ alloys at 0 K. The calculated properties serve as input to K_I -controlled simulations of fracture of the hexagonal alloys.

In atomistic modelling of fracture, the critical stress intensity K_{Ic} corresponds to the onset of unstable crack growth. For an ordered brittle crystal, such as TiN, the atomically-sharp crack extends on a straight path [35] at a stress intensity $K_{Ic} \approx (1+\epsilon) \cdot K_{Ic}^G$, where K_{Ic}^G is the thermodynamic Griffith value of mode-I toughness and the scalar ϵ (≈ 0.2) arises from lattice trapping of brittle cracks [96-98]. At variance with Ref. [35], here we have developed an algorithm that follows the movement of the crack tip. This allows us to determine conditions of unstable crack growth in $Ti_{1-x}Al_xN$. In these alloys, the formation of plastic zones complicates the analysis of σ_f and K_{Ic} fracture properties. At each K_I step, the position of the crack tip is (re)located considering the maximum atom-resolved stress and geometric descriptors that control changes in bond angles and bond lengths proximate to the identified position of maximum stress. This ensures an accurate definition of K_I during crack extension [34]. **Videos #1 and #5, #6, and #7** illustrate how the algorithm traces the crack tip movement in TiN(001) and $Ti_{0.4}Al_{0.6}N(001)$.

5.3. Determination of K_{Ic}^∞ and σ_f^∞ . K_I -controlled MS simulations provide tensile stress σ_{zz} vs stress-intensity K_I data (**Figure S10 and S11**) for each simulated plate model of area A . The $\sigma_{zz}(K_I)$ curve exhibits linear dependence on K_I up to stress intensity values near the onset of plastic deformation or fracture. We analyze σ_{zz} vs. K_I data for stress intensities in the range $0 \leq K_I \leq K_I^{5\%} + \Delta K$ (with $\Delta K \ll K_I^{5\%}$). The threshold value $K_I^{5\%}$ corresponds to a lateral advancement of the crack tip (Δ_{tip}), or extension of the secondary B_k phase, equal to 5% of the supercell width. The criterion is based on the observation that all investigated alloys exhibit either unstable crack extension or rapid phase transformation at $K_I \approx K_I^{5\%}$. Then, we locate the maximum stress $\sigma_{zz}^{\max}(\tilde{K}_I)$ value within the stress-intensity interval $0 < \tilde{K}_I \leq K_I^{5\%}$. This allows

us to define the fracture strength $\sigma_f \equiv \sigma_{zz}^{\max}(\tilde{K}_I)$ and fracture toughness $K_{Ic} \equiv \tilde{K}_I$ for each plate area A . Visualization of the simulations, supported by analyses of σ_{zz} and Δ_{tip} trends as a function of K_I , confirms that the definitions of σ_f and K_{Ic} are physically meaningful.

Atomistic predictions of fracture properties are spuriously affected by limited supercell sizes and boundary conditions [99]. Here, we circumvent these problems by explicitly considering the dependence of fracture properties on the size of supercell models. As expected, the calculated fracture properties vary smoothly with the area of the cracked plate. Accordingly, the fracture toughness and fracture strength reach asymptotic values K_{Ic}^∞ and σ_f^∞ for $A \rightarrow \infty$. Spurious effects caused by boundary conditions are also expected to vanish at the limit of infinite sizes. Hence, K_{Ic}^∞ and σ_f^∞ are extrapolated by using constitutive scaling laws that reproduce trends in K_{Ic} and σ_f as a function of A (see also **Section S1 of the SI**).

The values K_{Ic}^∞ obtained by atomistic simulations of fracture are compared to the thermodynamic value K_{Ic}^G based on Griffith's theory of fracture. Griffith's formulation assumes a perfectly homogeneous elastic body containing a crack. Hence, the value of K_{Ic}^G for the cracked-plate problem is simply obtained from the cleavage energy and the Stroh energy tensor Λ , which can be calculated from the elastic constants tensor C_{ij} [34, 35] (more information in **Section S2 of the SI**). The elastic constants predicted by MS for B1 $\text{Ti}_{1-x}\text{Al}_x\text{N}$ have been taken from Ref. [33]. In this work, we also compute the elastic constants of hexagonal B_k $\text{Ti}_{0.25}\text{Al}_{0.75}\text{N}$, $\text{Ti}_{0.15}\text{Al}_{0.85}\text{N}$, and $\text{Ti}_{0.05}\text{Al}_{0.95}\text{N}$. The unrelaxed surface energies of $\text{Ti}_{1-x}\text{Al}_x\text{N}(001)$ are computed by MS and DFT using supercells with large areas (to minimize degree of short-range lattice ordering) and thickness of 6 layers. Calculations of surface energies are done as previously (see, e.g. [100]). The results of surface energies calculated by MS and DFT are summarized in **Table S1 of the SI**.

5.4. Transformation energies and degree of plastic deformation. The percentage of cubic and transformed (non-cubic) structures in mode-I deformed $\text{Ti}_{1-x}\text{Al}_x\text{N}$ cracked plate models is

determined using the common neighbor analysis (cutoff of 3.15 Å) as implemented in OVITO [101]. The energies of transformation from cubic B₁ to hexagonal B_k are determined as a function of the Al content along a transformation path schematically illustrated in **Figure 1c**. The calculations at a given Al content are repeated with several different cation arrangements. The B₁→B_k transformation energy landscapes are depicted in **Figure S6 of the SI**. Results obtained with the classical potential are supported by DFT calculations, which qualitatively show that the $\Delta E_{B_1 \rightarrow B_k}$ activation energy decreases for increasing Al content **Figure S7**.

Acknowledgements

The computations were enabled by resources provided by the National Academic Infrastructure for Supercomputing in Sweden (NAISS) at NSC in Linköping and PDC in Stockholm partially funded by the Swedish Research Council through Grant Agreements No. 2022-06725. Dr. Luis Casillas Trujillo at NSC is gratefully acknowledged for technical support. We gratefully acknowledge financial support from the Swedish Research Council (VR) through Grants No. VR-2021-04426 and No. 2023-05358, the Competence Center Functional Nanoscale Materials (FunMat-II) (Vinnova Grant No. 2022-03071), the Swedish Government Strategic Research Area in Materials Science on Functional Materials at Linköping University (Faculty Grant SFO-Mat-LiU Grant No. 2009-00971), and the Knut and Alice Wallenberg Foundation through Wallenberg Scholar project (Grant No. 2018.0194). This work is supported by ERC Grant UNMASCC-HP, 101117758, funded by the European Union. Views and opinions expressed are however those of the author(s) only and do not necessarily reflect those of the European Union or the European Research Council Executive Agency. Neither the European Union nor the granting authority can be held responsible for them.

References

- [1] R.H.J. Hannink, P.M. Kelly, B.C. Muddle, Transformation toughening in zirconia-containing ceramics, *Journal of the American Ceramic Society* 83 (2000) 461.
- [2] M. Trunec, Z. Chlup, Higher fracture toughness of tetragonal zirconia ceramics through nanocrystalline structure, *Scripta Materialia* 61 (2009) 56.
- [3] A. Bravo-Leon, Y. Morikawa, M. Kawahara, M.J. Mayo, Fracture toughness of nanocrystalline tetragonal zirconia with low yttria content, *Acta Materialia* 50 (2002) 4555.
- [4] K. Matsui, K. Hosoi, B. Feng, H. Yoshida, Y. Ikuhara, Ultrahigh toughness zirconia ceramics, *Proceedings of the National Academy of Sciences of the United States of America* 120 (2023) e2304498120.
- [5] P.M. Kelly, L.R.F. Rose, The martensitic transformation in ceramics - its role in transformation toughening, *Progress in Materials Science* 47 (2002) 463.
- [6] O. Gavaldà-Díaz, M. Emmanuel, K. Marquardt, E. Saiz, F. Giuliani, Observing the crack tip behaviour at the nanoscale during fracture of ceramics, *Proceedings of the National Academy of Sciences of the United States of America* 121 (2024) e2408292121.
- [7] J. Chevalier, L. Gremillard, A. Virkar, D. Clarke, The Tetragonal-Monoclinic Transformation in Zirconia: Lessons Learned and Future Trends, *Journal of the American Ceramic Society* 92 (2009) 1901.
- [8] G.N. Morscher, P. Pirouz, A.H. Heuer, Temperature-dependence of hardness in yttria-stabilized zirconia single-crystals, *Journal of the American Ceramic Society* 74 (1991) 491.
- [9] R.G. Wellman, A. Dyer, J.R. Nicholls, Nano and micro indentation studies of bulk zirconia and EB PVD TBCs, *Surface & Coatings Technology* 176 (2004) 253.
- [10] V. Tikare, A.H. Heuer, Temperature-dependent indentation behavior of transformation-toughened zirconia-based ceramics, *Journal of the American Ceramic Society* 74 (1991) 593.
- [11] M. Magalhaes, T. Douillard, H. Reveron, S. Comby-Dassonneville, T. Cornelius, S. Meille, M. Texier, J. Micha, D. Rodney, O. Thomas, J. Chevalier, In-situ Laue micro-diffraction during compression tests on Ce-TZP single crystal micropillars, *Journal of the European Ceramic Society* 45 (2025) 116794.
- [12] X. Luo, W. Zhou, S. Ushakov, A. Navrotsky, A. Demkov, Monoclinic to tetragonal transformations in hafnia and zirconia: A combined calorimetric and density functional study, *Physical Review B* 80 (2009) 134119.
- [13] S. Guan, X. Zhang, Z. Liu, Energy Landscape of Zirconia Phase Transitions, *Journal of the American Chemical Society* 137 (2015) 8010.
- [14] H. Kindlund, D.G. Sangiovanni, I. Petrov, J.E. Greene, L. Hultman, A review of the intrinsic ductility and toughness of hard transition-metal nitride alloy thin films, *Thin Solid Films* 688 (2019) 137479.
- [15] L.E. Toth, *Transition Metal Carbides and Nitrides*, Academic Press, New York (1971).
- [16] T. Glechner, R. Hahn, T. Wojcik, D. Holec, S. Koložsvári, H. Zaid, S. Kodambaka, P.H. Mayrhofer, H. Riedl, Assessment of ductile character in superhard Ta-CN thin films, *Acta Materialia* 179 (2019) 17.
- [17] Y.X. Xu, Y. Ding, B. Peng, Q. Zhang, Q. Wang, Hardening and toughening of Ti–Al–N thin films through the solid solution of Ni, *Surface & Coatings Technology* 493 (2024) 131283.
- [18] H. Waldl, M. Tkadletz, A. Lechner, C. Czettel, M. Pohler, N. Schalk, Evolution of the fracture properties of arc evaporated Ti_{1-x}Al_xN coatings with increasing Al content, *Surface & Coatings Technology* 444 (2022) 128690.
- [19] Y. Moritz, C. Kainz, M. Tkadletz, C. Czettel, M. Pohler, N. Schalk, Microstructure and mechanical properties of arc evaporated Ti(Al,Si)N coatings, *Surface & Coatings Technology* 421 (2021) 127461.
- [20] A. Riedl, R. Daniel, M. Stefanelli, T. Schoeberl, O. Kolednik, C. Mitterer, J. Keckes, A novel approach for determining fracture toughness of hard coatings on the micrometer scale, *Scripta Materialia* 67 (2012) 708.
- [21] D. Holec, R. Rachbauer, L. Chen, L. Wang, D. Luef, P.H. Mayrhofer, Phase stability and alloy-related trends in Ti-Al-N, Zr-Al-N and Hf-Al-N systems from first principles, *Surface & Coatings Technology* 206 (2011) 1698.

- [22] A. Siegel, K. Parlinski, U.D. Wdowik, Ab initio calculation of structural phase transitions in AlN crystal, *Physical Review B* 74 (2006) 104116.
- [23] N. Shulumba, O. Hellman, Z. Raza, B. Alling, J. Barrirero, F. Muecklich, I.A. Abrikosov, M. Oden, Lattice Vibrations Change the Solid Solubility of an Alloy at High Temperatures, *Physical Review Letters* 117 (2016) 205502.
- [24] D.G. Sangiovanni, Mass transport properties of quasiharmonic vs. anharmonic transition-metal nitrides, *Thin Solid Films* 688 (2019) 137297.
- [25] D. Gambino, D.G. Sangiovanni, B. Alling, I.A. Abrikosov, Nonequilibrium ab initio molecular dynamics determination of Ti monovacancy migration rates in B1 TiN, *Physical Review B* 96 (2017) 104306.
- [26] L. Hultman, Thermal stability of nitride thin films, *Vacuum* 57 (2000) 1.
- [27] J. Zhou, J. Zhong, L. Chen, L. Zhang, Y. Du, Z.-K. Liu, P.H. Mayrhofer, Phase equilibria, thermodynamics and microstructure simulation of metastable spinodal decomposition in c-Ti_{1-x}Al_xN coatings, *CALPHAD* 56 (2017) 92.
- [28] K. Yalamanchili, I.C. Schramm, E. Jimenez-Pique, L. Rogstrom, F. Muecklich, M. Oden, N. Ghafoor, Tuning hardness and fracture resistance of ZrN/Zr_{0.63}Al_{0.37}N nanoscale multilayers by stress-induced transformation toughening, *Acta Materialia* 89 (2015) 22.
- [29] M. Schloegl, C. Kirchlechner, J. Paulitsch, J. Keckes, P.H. Mayrhofer, Effects of structure and interfaces on fracture toughness of CrN/AlN multilayer coatings, *Scripta Materialia* 68 (2013) 917.
- [30] M. Bartosik, C. Rumeau, R. Hahn, Z.L. Zhang, P.H. Mayrhofer, Fracture toughness and structural evolution in the TiAlN system upon annealing, *Scientific Reports* 7 (2017) 16476.
- [31] G. Greczynski, L. Hultman, M. Odén, X-ray photoelectron spectroscopy studies of Ti_{1-x}Al_xN (0 ≤ x ≤ 0.83) high-temperature oxidation: The crucial role of Al concentration, *Surface & Coatings Technology* 374 (2019) 923.
- [32] I. Endler, M. Höhn, M. Herrmann, R. Pitonak, S. Ruppi, M. Schneider, H. van den Berg, H. Westphal, Novel aluminum-rich Ti_{1-x}Al_xN coatings by LPCVD, *Surface & Coatings Technology* 203 (2008) 530.
- [33] G.A. Almyras, D.G. Sangiovanni, K. Sarakinos, Semi-Empirical Force-Field Model for the Ti_{1-x}Al_xN (0 ≤ x ≤ 1) System, *Materials* 12 (2019) 215.
- [34] P. Andric, W.A. Curtin, Atomistic modeling of fracture, *Modelling and Simulation in Materials Science and Engineering* 27 (2019) 013001.
- [35] D.G. Sangiovanni, A. Kraych, M. Mrovec, J. Salamania, M. Oden, F. Tasnadi, I.A. Abrikosov, Descriptor for slip-induced crack blunting in refractory ceramics, *Physical Review Materials* 7 (2023) 103601.
- [36] L. Huang, F. Zheng, Q. Deng, Q. Thi, L. Wong, Y. Cai, N. Wang, C. Lee, S. Lau, M. Chhowalla, J. Li, T. Ly, J. Zhao, In Situ Scanning Transmission Electron Microscopy Observations of Fracture at the Atomic Scale, *Physical Review Letters* 125 (2020) 246102.
- [37] B. Lawn, B. Hockey, S. Wiederhorn, Atomically sharp cracks in brittle solids - an electron-microscopy study, *Journal of Materials Science* 15 (1980) 1207.
- [38] H. Tanaka, Y. Bando, Y. Inomata, M. Mitomo, Atomically sharp crack in 15R-SiAlON, *Journal of the American Ceramic Society* 71 (1988) C32.
- [39] S. Wang, Z. Qin, G. Jung, F. Martin-Martinez, K. Zhang, M. Buehler, J. Warner, Atomically Sharp Crack Tips in Monolayer MoS₂ and Their Enhanced Toughness by Vacancy Defects, *ACS Nano* 10 (2016) 9831.
- [40] J. Salamania, D.G. Sangiovanni, A. Kraych, K.M.C. Kwick, I.C. Schramm, L.J.S. Johnson, R. Boyd, B. Bakhit, T.W. Hsu, M. Mrovec, Elucidating dislocation core structures in titanium nitride through high-resolution imaging and atomistic simulations, *Materials & Design* 224 (2022) 111327.
- [41] Z. Chen, Y. Zheng, L. Loeffler, M. Bartosik, G.K. Nayak, O. Renk, D. Holec, P.H. Mayrhofer, Z. Zhang, Atomic insights on intermixing of nanoscale nitride multilayer triggered by nanoindentation, *Acta Materialia* 214 (2021) 117004.
- [42] N. Koutná, L. Löffler, D. Holec, Z. Chen, Z. Zhang, L. Hultman, P.H. Mayrhofer, D.G. Sangiovanni, Atomistic mechanisms underlying plasticity and crack growth in ceramics: a case study of AlN/TiN superlattices, *Acta Materialia* 229 (2022) 117809.

- [43] J. Salamania, F. Bock, L.J.S. Johnson, F. Tasnadi, K.M. Calamba Kwick, A.F. Farhadizadeh, I.A. Abrikosov, L. Rogström, M. Odén, High temperature decomposition and age hardening of single-phase wurtzite $Ti_{1-x}Al_xN$ thin films grown by cathodic arc deposition, *Physical Review Materials* 8 (2024) 013602.
- [44] M. Ben Hassine, H. Andrén, A. Iyer, A. Lotsari, O. Bäcke, D. Stiens, W. Janssen, T. Manns, J. Kümmel, M. Halvarsson, Growth model for high-Al containing CVD TiAlN coatings on cemented carbides using intermediate layers of TiN, *Surface & Coatings Technology* 421 (2021) 127361.
- [45] H. Levämäki, F. Tasnadi, D.G. Sangiovanni, L.J.S. Johnson, R. Armiento, I.A. Abrikosov, Predicting elastic properties of hard-coating alloys using ab-initio and machine learning methods, *npj Computational Materials* 8 (2022) 17.
- [46] W. Liu, X. Liu, W.T. Zheng, Q. Jiang, Surface energies of several ceramics with NaCl structure, *Surface Science* 600 (2006) 257.
- [47] A. Forslund, A. Ruban, Surface energetics of $Al_xTi_{1-x}N$ alloys, *Computational Materials Science* 183 (2020) 109813.
- [48] D.G. Sangiovanni, D. Edström, L. Hultman, V. Chirita, I. Petrov, J.E. Greene, Dynamics of Ti, N, and TiN_x ($x = 1-3$) admolecule transport on $TiN(001)$ surfaces, *Physical Review B* 86 (2012) 155443.
- [49] R.O. Ritchie, The conflicts between strength and toughness, *Nature Materials* 10 (2011) 817.
- [50] F.F. Ge, H.S. Sen, N. Daghbouj, M. Callisti, Y.J. Feng, B.S. Li, P. Zhu, P. Li, F.P. Meng, T. Polcar, Toughening mechanisms in V-Si-N coatings, *Materials & Design* 209 (2021) 109961.
- [51] J. Salamania, K.M.C. Kwick, D.G. Sangiovanni, F. Tasnadi, I.A. Abrikosov, L. Rogstrom, L.J.S. Johnson, M. Oden, High-resolution STEM investigation of the role of dislocations during decomposition of $Ti_{1-x}Al_xN_y$, *Scripta Materialia* 229 (2023) 115366.
- [52] P. Andric, W.A. Curtin, New theory for Mode I crack-tip dislocation emission, *Journal of the Mechanics and Physics of Solids* 106 (2017) 315.
- [53] C. Kainz, N. Schalk, M. Tkadletz, C. Mitterer, C. Czettel, Microstructure and mechanical properties of CVD TiN/TiBN multilayer coatings, *Surface & Coatings Technology* 370 (2019) 311.
- [54] R. Daniel, M. Meindlhumer, W. Baumegger, J. Zalesak, B. Sartory, M. Burghammer, C. Mitterer, J. Keckes, Grain boundary design of thin films: Using tilted brittle interfaces for multiple crack deflection toughening, *Acta Materialia* 122 (2017) 130.
- [55] S. Massl, W. Thomma, J. Keckes, R. Pippan, Investigation of fracture properties of magnetron-sputtered TiN films by means of a FIB-based cantilever bending technique, *Acta Materialia* 57 (2009) 1768.
- [56] J. Buchinger, L. Löfler, J. Ast, A. Wagner, Z. Chen, J. Michler, Z.L. Zhang, P.H. Mayrhofer, D. Holec, M. Bartosik, Fracture properties of thin film TiN at elevated temperatures, *Materials & Design* 194 (2020) 108885.
- [57] B. Völker, C. Du, H. Fager, H. Ruess, R. Soler, C. Kirchlechner, G. Dehm, J. Schneider, How tensile tests allow a screening of the fracture toughness of hard coatings, *Surface & Coatings Technology* 390 (2020) 125645.
- [58] W.M. Seidl, M. Bartosik, S. Kolozsvari, H. Bolvardi, P.H. Mayrhofer, Influence of Ta on the fracture toughness of arc evaporated Ti-Al-N, *Vacuum* 150 (2018) 24.
- [59] B. Kaygusuz, A. Motallebzadeh, Ö. Karadayi, K. Kazmanli, S. Özerinç, Fracture toughness of AlTiN coatings investigated by nanoindentation and microcantilever bending, *Thin Solid Films* 790 (2024) 140199.
- [60] J. Best, J. Wehrs, M. Polyakov, M. Morstein, J. Michler, High temperature fracture toughness of ceramic coatings evaluated using micro-pillar splitting, *Scripta Materialia* 162 (2019) 190.
- [61] Z.L. Zhang, A. Ghasemi, N. Koutna, Z. Xu, T. Grunstaedl, K.X. Song, D. Holec, Y.B. He, P.H. Mayrhofer, M. Bartosik, Correlating point defects with mechanical properties in nanocrystalline TiN thin films, *Materials & Design* 207 (2021) 109844.
- [62] P.L. Larsson, A.E. Giannakopoulos, Tensile stresses and their implication to cracking at pyramid indentation of pressure-sensitive hard metals and ceramics, *Materials Science and Engineering A* 254 (1998) 268.

- [63] R. Rice, Grain size and porosity dependence of ceramic fracture energy and toughness at 22 degrees °C, *Journal of Materials Science* 31 (1996) 1969.
- [64] C. Fuger, R. Hahn, A. Hirle, P. Kutrowatz, M. Weiss, A. Limbeck, O. Hunold, P. Polcik, H. Riedl, Revisiting the origins of super-hardness in TiB_{2+z} thin films-Impact of growth conditions and anisotropy, *Surface & Coatings Technology* 446 (2022) 128806.
- [65] L. Tan, T. Allen, P. Demkowicz, High temperature interfacial reactions of TiC, ZrC, TiN, and ZrN with palladium, *Solid State Ionics* 181 (2010) 1156.
- [66] K. Merkle, D. Smith, Atomic-structure of symmetrical tilt grain-boundaries in NiO, *Physical Review Letters* 59 (1987) 2887.
- [67] J. Bean, M. Saito, S. Fukami, H. Sato, S. Ikeda, H. Ohno, Y. Ikuhara, K. McKenna, Atomic structure and electronic properties of MgO grain boundaries in tunnelling magnetoresistive devices, *Scientific Reports* 7 (2017) 45594.
- [68] Z. Wang, M. Saito, K.P. McKenna, L. Gu, S. Tsukimoto, A.L. Shluger, Y. Ikuhara, Atom-resolved imaging of ordered defect superstructures at individual grain boundaries, *Nature* 479 (2011) 380.
- [69] S. Li, C. Sun, H. Park, Grain boundary structures of atomic layer deposited TiN, *Thin Solid Films* 504 (2006) 108.
- [70] D. Edström, D.G. Sangiovanni, L. Hultman, I. Petrov, J.E. Greene, V. Chirita, Large-scale molecular dynamics simulations of TiN/TiN(001) epitaxial film growth, *Journal of Vacuum Science & Technology A* 34 (2016) 041509.
- [71] S. Yang, T. Guo, X. Yan, K. Gao, J. Qiu, X. Pang, Nanotwinned transition metal nitride coating with excellent thermal stability, *Acta Materialia* 267 (2024) 119743.
- [72] L. Zhang, Y. Liang, J. Gu, X. Yan, X. Li, P. Yu, L. Wang, Synthesis of nano (Ti,W)C powder with preferred orientation and twin boundary structure, *Advanced Powder Technology* 33 (2022) 103550.
- [73] Z. Xu, Z. Zhang, M. Bartosik, Y. Zhang, P. Mayrhofer, Y. He, Insight into the structural evolution during TiN film growth via atomic resolution TEM, *Journal of Alloys and Compounds* 754 (2018) 257.
- [74] Q. He, D. Liu, Y. Zhou, T.-Y. Sun, L.-F. Huang, Nitride coatings for environmental barriers: the key microscopic mechanisms and momentous applications of first-principles calculations, *Surface Science and Technology* 2 (2024) 24.
- [75] Z. Chen, Y. Zheng, L. Löfler, M. Bartosik, H. Sheng, C. Gammer, D. Holec, Z. Zhang, Real-time atomic-resolution observation of coherent twin boundary migration in CrN, *Acta Materialia* 208 (2021) 116732.
- [76] M. Saito, Z. Wang, Y. Ikuhara, Selective impurity segregation at a near-Σ5 grain boundary in MgO, *Journal of Materials Science* 49 (2014) 3956.
- [77] S. Wang, Y. Kong, L. Chen, Y. Du, Effect of Al content on the structural stability of Σ3 (111) twin boundary in Ti_{1-x}Al_xN hard coatings: A first-principles study, *Surface & Coatings Technology* 439 (2022) 128454.
- [78] M.N. Popov, A.S. Bochkarev, V.I. Razumovskiy, P. Puschnig, J. Spitaler, Point defects at the Σ5 (012)[100] grain boundary in TiN and the early stages of Cu diffusion: An ab initio study, *Acta Materialia* 144 (2018) 496.
- [79] L. Triestram, J. Polfus, Hydride ion diffusion along grain boundaries in titanium nitride, *Acta Materialia* 270 (2024) 119853.
- [80] K. McKenna, Structure, electronic properties, and oxygen incorporation/diffusion characteristics of the Σ5 TiN(310)[001] tilt grain boundary, *Journal of Applied Physics* 123 (2018) 075301.
- [81] Q. He, T. Sun, L. Huang, Chemical-bonding and lattice-deformation mechanisms unifying the stability and diffusion trends of hydrogen in TiN and AlN polymorphs, *Acta Materialia* 281 (2024) 120447.
- [82] A. Hörling, L. Hultman, M. Oden, J. Sjölen, L. Karlsson, Mechanical properties and machining performance of Ti_{1-x}Al_xN-coated cutting tools, *Surface & Coatings Technology* 191 (2005) 384.
- [83] C. Shen, J. Li, T. Niu, J. Cho, Z. Shang, Y. Zhang, A. Shang, B. Yang, K. Xu, R. Garcia, H. Wang, X. Zhang, Achieving room temperature plasticity in brittle ceramics through elevated temperature preloading, *Science Advances* 10 (2024) eadj4079.

- [84] L. Porz, A.J. Klomp, X.F. Fang, N. Li, C. Yildirim, C. Detlefs, E. Bruder, M. Hofling, W. Rheinheimer, E.A. Patterson, P. Gao, K. Durst, A. Nakamura, K. Albe, H. Simons, J. Rodel, Dislocation-toughened ceramics, *Materials Horizons* 8 (2021) 1528.
- [85] L. Dong, J. Zhang, Y. Li, Y. Gao, M. Wang, M. Huang, J. Wang, K. Chen, Borrowed dislocations for ductility in ceramics, *Science* 385 (2024) 422.
- [86] G. Kresse, J. Furthmuller, Efficient iterative schemes for ab initio total-energy calculations using a plane-wave basis set, *Physical Review B* 54 (1996) 11169.
- [87] G. Kresse, D. Joubert, From ultrasoft pseudopotentials to the projector augmented-wave method, *Physical Review B* 59 (1999) 1758.
- [88] J.P. Perdew, K. Burke, M. Ernzerhof, Generalized gradient approximation made simple, *Physical Review Letters* 77 (1996) 3865.
- [89] A.P. Thompson, H.M. Aktulga, R. Berger, D.S. Bolintineanu, W.M. Brown, P.S. Crozier, P.J. in 't Veld, A. Kohlmeyer, S.G. Moore, T.D. Nguyen, R. Shan, M.J. Stevens, J. Tranchida, C. Trott, S.J. Plimpton, LAMMPS-a flexible simulation tool for particle-based materials modeling at the atomic, meso, and continuum scales, *Computer Physics Communications* 271 (2022) 108171.
- [90] B.J. Lee, M.I. Baskes, Second nearest-neighbor modified embedded-atom-method potential, *Physical Review B* 62 (2000) 8564.
- [91] W. Humphrey, A. Dalke, K. Schulten, VMD: Visual molecular dynamics, *Journal of Molecular Graphics & Modelling* 14 (1996) 33.
- [92] A. Horling, L. Hultman, M. Oden, J. Sjolen, L. Karlsson, Thermal stability of arc evaporated high aluminum-content Ti_{1-x}Al_xN thin films, *Journal of Vacuum Science & Technology A* 20 (2002) 1815.
- [93] S. Aghda, D. Holzzapfel, D. Music, Y. Unutulmazsoy, S. Mráz, D. Bogdanovski, G. Fidanboy, M. Hans, D. Primetzhofer, A. Méndez, A. Anders, J. Schneider, Ion kinetic energy- and ion flux-dependent mechanical properties and thermal stability of (Ti,Al)N thin films, *Acta Materialia* 250 (2023) 118864.
- [94] S. Carvalho, E. Ribeiro, L. Rebouta, J. Pacaud, P. Goudeau, P. Renault, J. Rivière, C. Tavares, PVD grown (Ti,Si,Al)N nanocomposite coatings and (Ti,Al)N/(Ti,Si)N multilayers: structural and mechanical properties, *Surface & Coatings Technology* 172 (2003) 109.
- [95] D. Gall, S. Kodambaka, M.A. Wall, I. Petrov, J.E. Greene, Pathways of atomistic processes on TiN(001) and (111) surfaces during film growth: an ab initio study, *Journal of Applied Physics* 93 (2003) 9086.
- [96] J. Sinclair, Influence of interatomic force law and of kinks on propagation of brittle cracks, *Philosophical Magazine* 31 (1975) 647.
- [97] D. Holland, M. Marder, Cracks and atoms, *Advanced Materials* 11 (1999) 793.
- [98] M. Marder, Particle methods in the study of fracture, *International Journal of Fracture* 196 (2015) 169.
- [99] M. Buze, J. Kermode, Numerical-continuation-enhanced flexible boundary condition scheme applied to mode-I and mode-III fracture, *Physical Review E* 103 (2021) 033002.
- [100] D.G. Sangiovanni, F. Tasnadi, L. Hultman, I. Petrov, J.E. Greene, V. Chirita, N and Ti adatom dynamics on stoichiometric polar TiN(111) surfaces, *Surface Science* 649 (2016) 72.
- [101] A. Stukowski, Visualization and analysis of atomistic simulation data with OVITO-the Open Visualization Tool, *Modelling and Simulation in Materials Science and Engineering* 18 (2010) 015012.

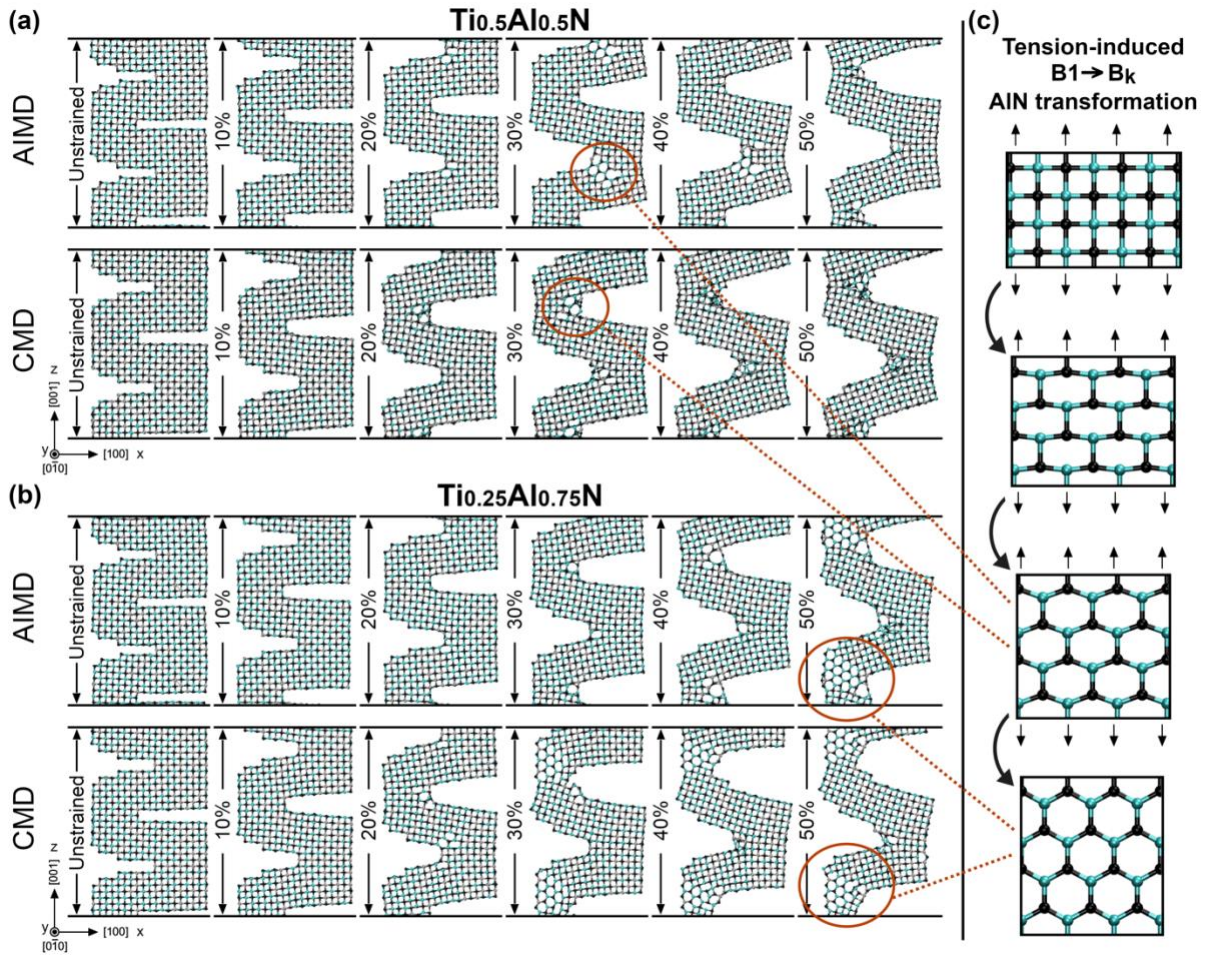


Figure 1. AIMD and CMD results of B1-structured bi-notched (a) $\text{Ti}_{0.5}\text{Al}_{0.5}\text{N}$ and (b) $\text{Ti}_{0.25}\text{Al}_{0.75}\text{N}$ supercell models subject to [001] elongation at 300 K. The structures are periodic along the y and z Cartesian directions. Vacuum regions separate supercell replicas along x. During AIMD simulations, self-healing of the notches is prevented by keeping eight helium atoms (not shown) at fixed position in the middle of the cavities. N, Al, and Ti atoms are colored in black, cyan, and silver, respectively. (c) Schematic representation of tension-induced $\text{B1} \rightarrow \text{B}_k$ transformation in AlN. Orange circles and dashed lines indicate formation of B_k -like environments near the notches of vertically-elongated $\text{Ti}_{0.5}\text{Al}_{0.5}\text{N}$ and $\text{Ti}_{0.25}\text{Al}_{0.75}\text{N}$ supercells.

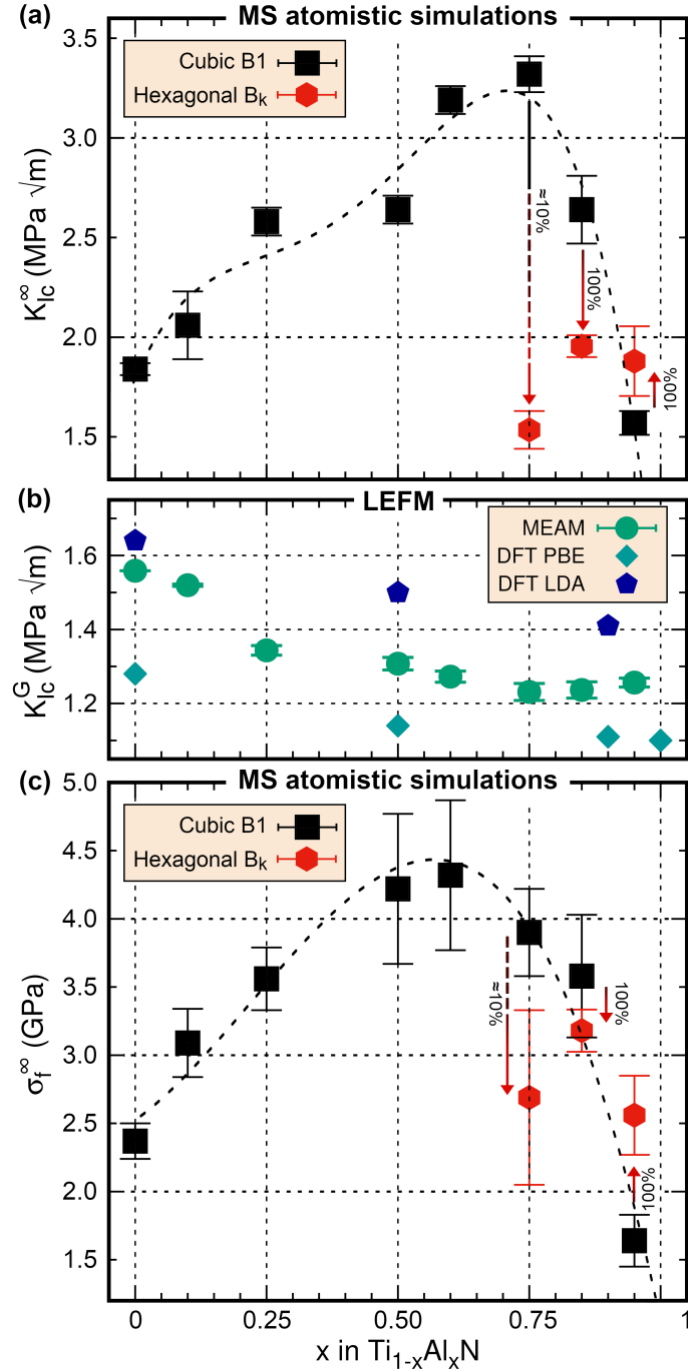


Figure 2. (a) Macroscale fracture toughness (K_{Ic}^∞) and (c) macroscale fracture strength (σ_f^∞) of $\text{Ti}_{1-x}\text{Al}_x\text{N}$ lattice models computed by MS K_I -controlled simulations as a function of the Al content x . Values of single-phase B1 $\text{Ti}_{1-x}\text{Al}_x\text{N}(001)$ are indicated by black squares. Red hexagons are mean values of fracture properties obtained for single-phase B_k $\text{Ti}_{1-x}\text{Al}_x\text{N}$ with cracks on (1100) and (1120) planes. The vertical red arrows (labeled with percentages) indicate the probability of observing the B1→B_k phase transformation during simulations of Al-rich ($x > 0.7$) alloys. The dashed curved black lines guide the eye across calculated trends. The extrapolated infinite-size values of K_{Ic}^∞ and σ_f^∞ are obtained by fitting K_{Ic} and σ_f results collected for different plate areas (see Section S1 in the SI). For comparison with results in (a), panel (b) shows the fracture toughness (K_{Ic}^G) values based on anisotropic linear elastic fracture mechanics (Griffith's theory). The alloys' unrelaxed surface energies $E^{(001)}$ and Stroh matrix elements Λ_{22}^{-1} used for determination of Griffith's fracture toughness ($K_{Ic}^G = \sqrt{[2 \cdot E^{(001)} \cdot \Lambda_{22}^{-1}]}$) are obtained by both MS and DFT calculations (see Section S2 in the SI).

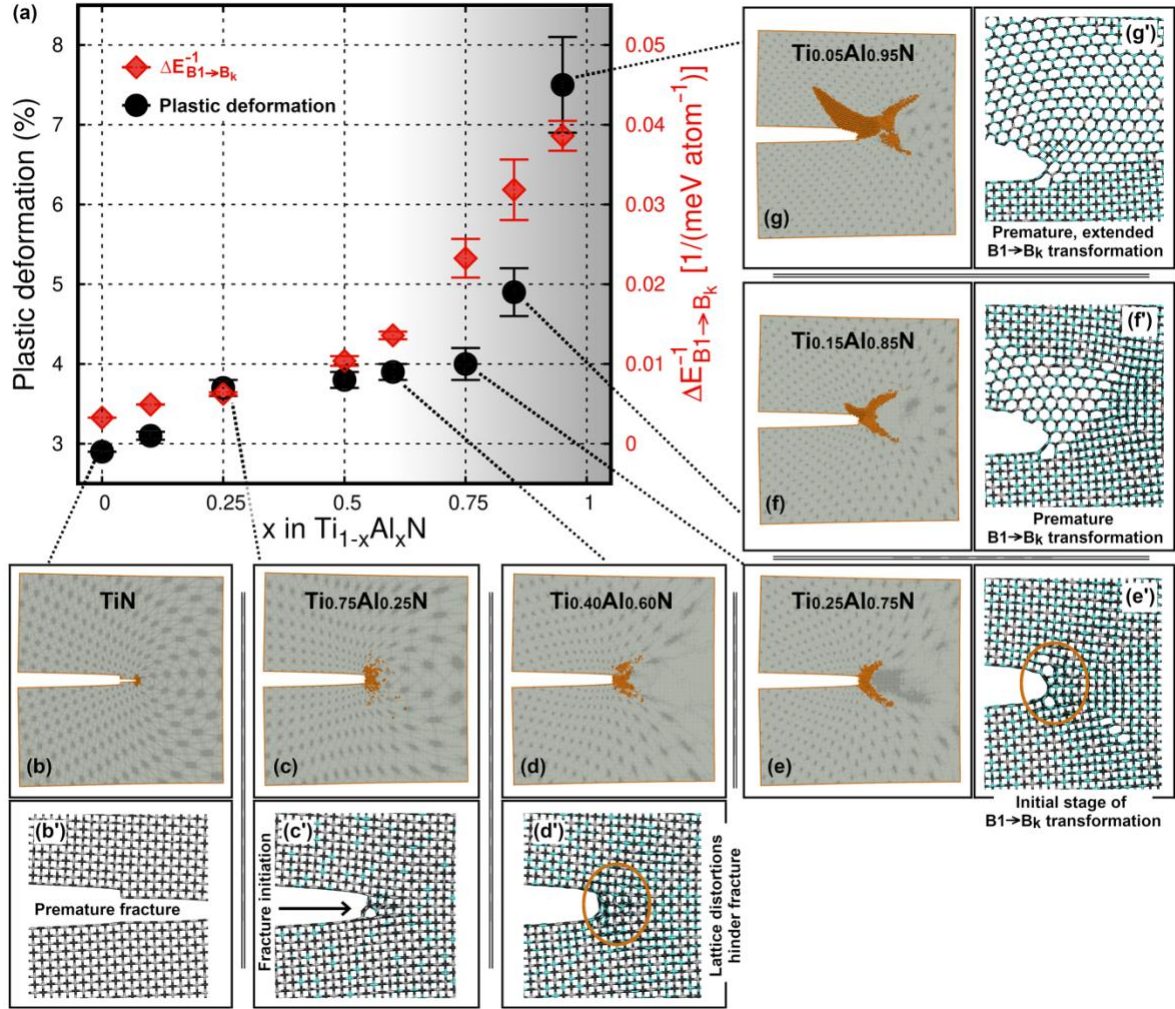


Figure 3. (a) Correlation between percentage of plastic deformation and inverse of the energy barrier $\Delta E_{B1 \rightarrow Bk}$ for cubic-to-hexagonal Ti_{1-x}Al_xN transformation separately calculated for 3D-periodic supercells. The energy landscape along B1 \rightarrow B_k transformation paths are shown in **Figure S6 of the SI**. The percentage of transformed (non-cubic) lattice structure is determined using the common neighbor analysis on Ti_{1-x}Al_xN plate models of area $A \approx 1800 \text{ nm}^2$ (shown in (b-g)) at a stress-intensity factor $K_I = 2 \text{ MPa} \sqrt{\text{m}}$. In (a), the white-gray color gradient at $x \approx 0.6$ indicates that both strength and toughness are initially positively affected by plasticity (white region), while they decrease for $x > 0.7$ (darker shade) due to premature stress-activated transformation. Atomistic models shown in (b-g) highlight relative portions of pristine B1-structured lattices (gray) as well as non-cubic plastically-deformed environments (orange). Panels (b'-g') are magnifications of regions around the crack tip, where N, Al, and Ti atoms are colored in black, cyan, and silver, respectively.

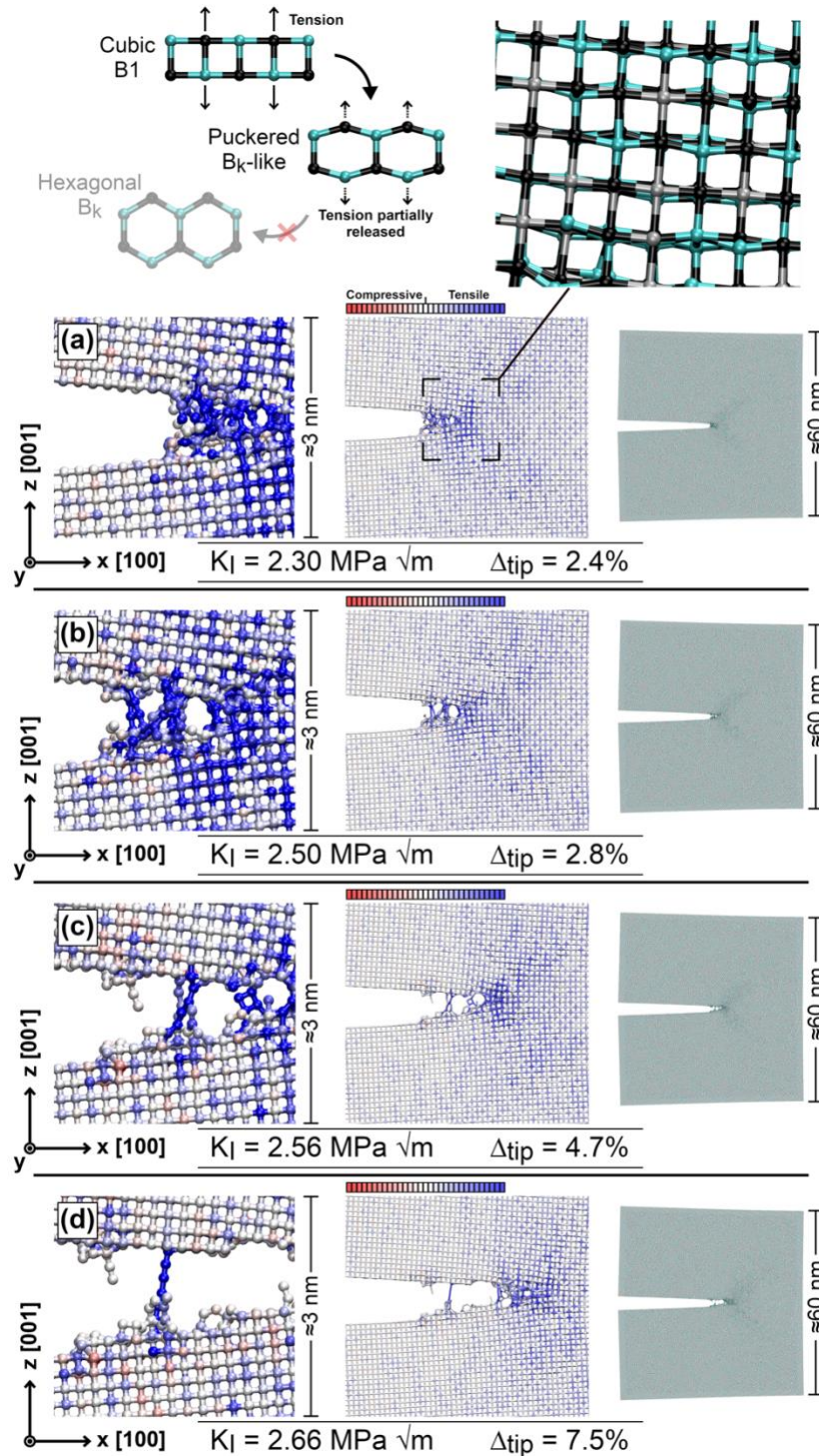


Figure 4. Al-induced strengthening and toughening mechanism in B1 $\text{Ti}_{1-x}\text{Al}_x\text{N}$. The figure shows as illustrative case a $\text{Ti}_{0.4}\text{Al}_{0.6}\text{N}$ cracked plate model with area $\approx 3600 \text{ nm}^2$. Note that atoms are colored according to the local tensile stress (see legend). **(a)** Formation of B_k -like domains around the crack tip at a stress-intensity factor $K_I = 2.30 \text{ MPa } \sqrt{\text{m}}$, which corresponds to a lateral advancement (Δ_{tip}) of the tip of 2.4%. **(b,c,d)** Formation of ligaments with high load-carrying capacity. Acting behind the crack tip, the ligaments effectively toughen the alloy by obstructing crack propagation.

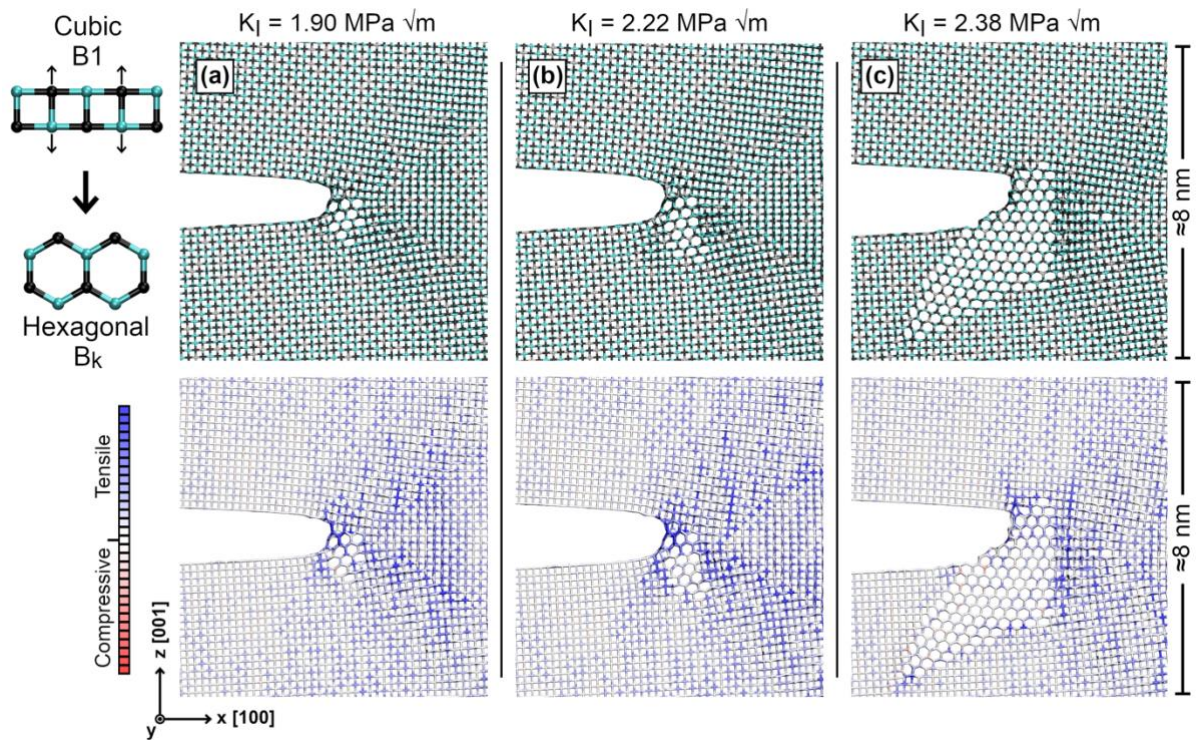


Figure 5. Simulation snapshots of B1-structured $\text{Ti}_{0.15}\text{Al}_{0.85}\text{N}(001)$ that locally transforms into B_k during mode-I loading. The stress intensity factors indicated at the top are referenced to the B1 structure.

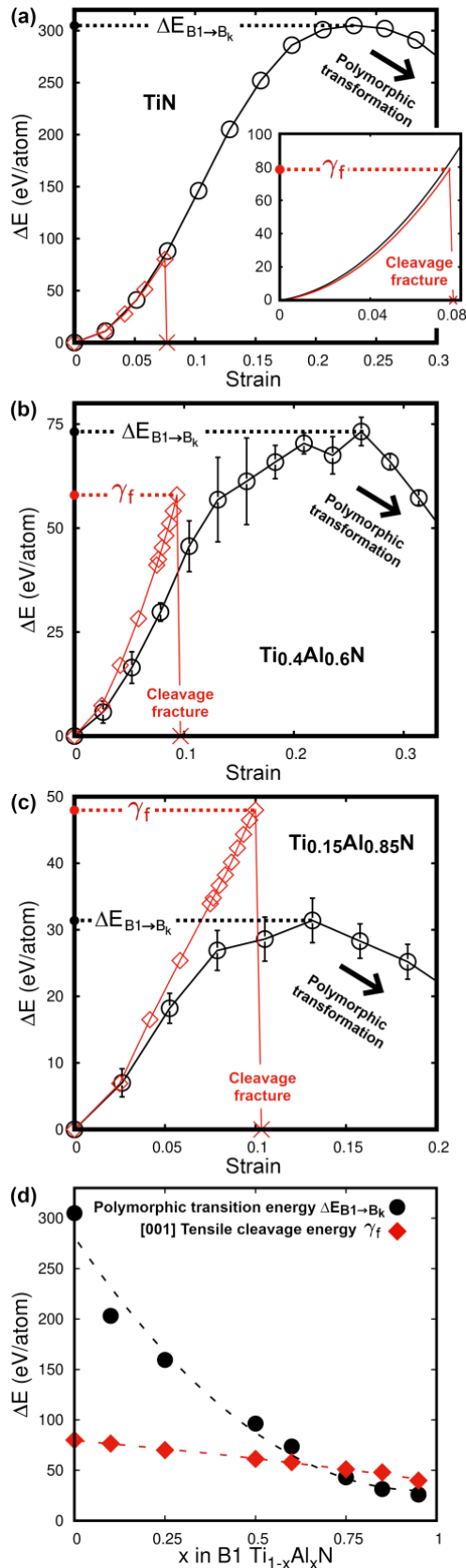


Figure 6. (a-c) Energetic competition between uniform tensile elongation along the [001] direction (red diamonds) and B1 \rightarrow B_k polymorphic transformation energy (black circles) along the path shown in **Figure 1c**. Calculation details are given in **Section S3 of the SI**. The activation energies for B1 \rightarrow B_k transformation and cleavage fracture of B1 Ti_{1-x}Al_xN alloys on a {001} plane are summarized in (d).

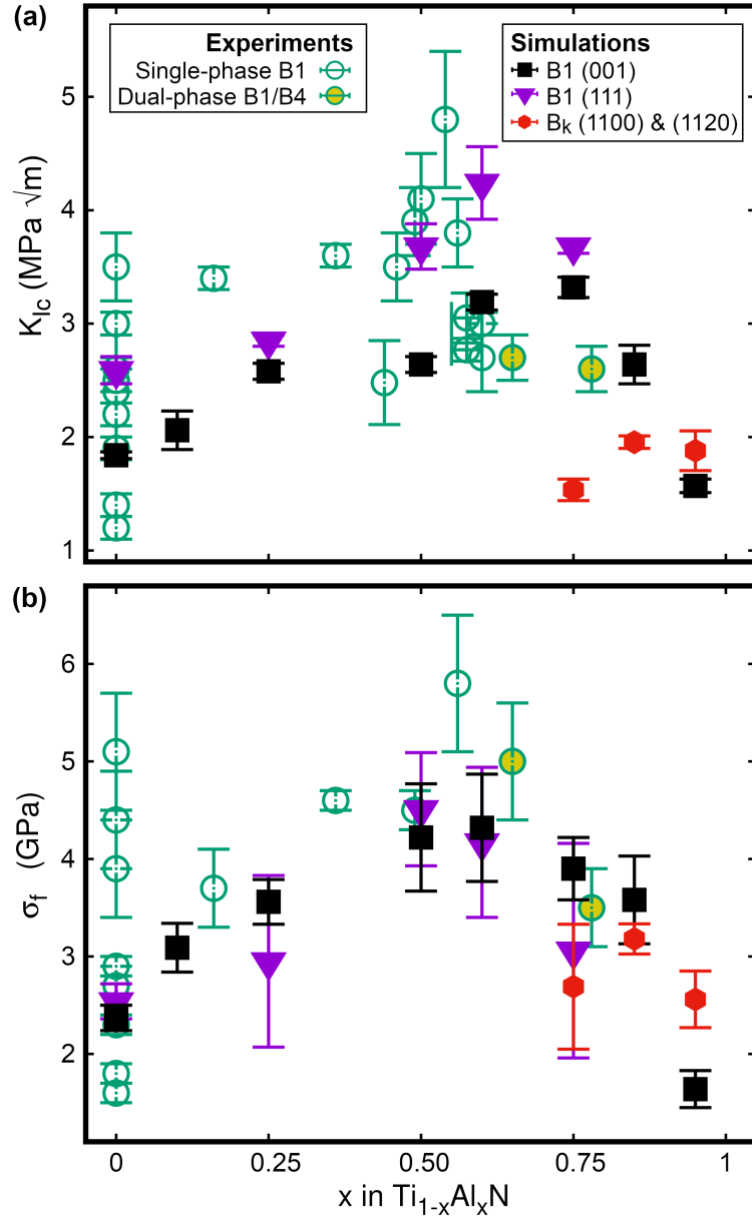


Figure 7. Comparison between fracture toughness K_{Ic}^{∞} and fracture strength σ_f^{∞} obtained by K_I -controlled simulations with fracture properties obtained by microcantilever bending and micropillar splitting of $\text{Ti}_{1-x}\text{Al}_x\text{N}$ as a function x . Note that experimental data colored in yellow were collected for dual-phase B1/B4 $\text{Ti}_{1-x}\text{Al}_x\text{N}$ [18]. The labels “B1 (001)”, “B1 (111)”, and “ B_k (1100) & (1120)” indicate simulation results obtained for B1-structured and B_k -structured $\text{Ti}_{1-x}\text{Al}_x\text{N}$ cracked plate models with atomically-sharp cracks on (001), (111), (1100) and (1120) planes. The results of simulations on B1 $\text{Ti}_{1-x}\text{Al}_x\text{N}$ (001) and B_k $\text{Ti}_{1-x}\text{Al}_x\text{N}$ are also shown in **Figure 2a,c**.

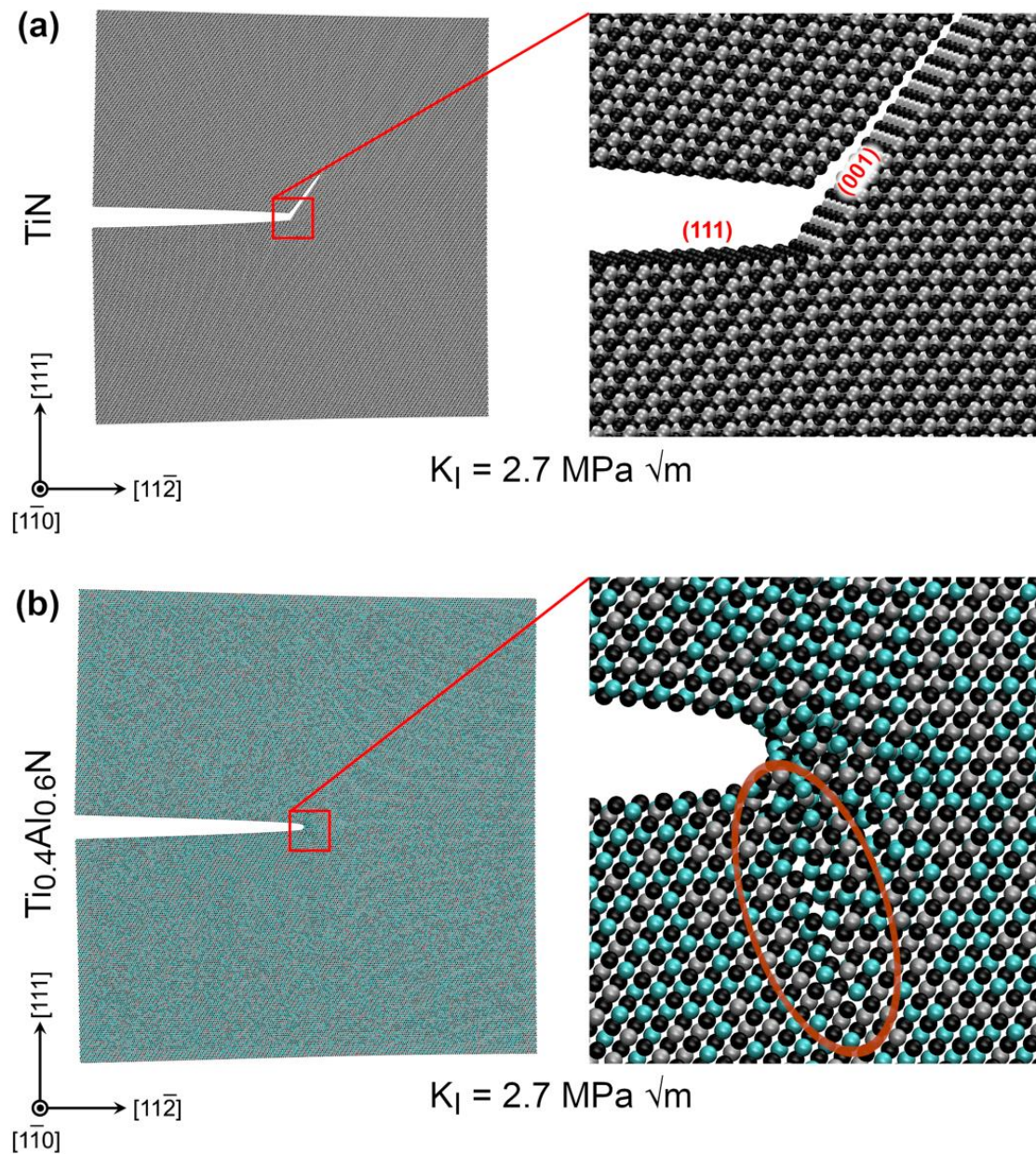


Figure 8. Simulation snapshots of $\text{Ti}_{1-x}\text{Al}_x\text{N}(111)$ cracked plate models subjected to mode-I loading. **(a)** An atomically-sharp crack on a $\{111\}$ plane of TiN is readily deflected on a $\{001\}$ plane. **(b)** Mode-I loading of $\text{Ti}_{0.4}\text{Al}_{0.6}\text{N}(111)$ induces nucleation and emission of a dislocation, indicated by the orange circle. N, Al, and Ti atoms are colored in black, cyan, and silver, respectively.